Title

Anisotropy beneath a highly extended continental rift

Journal

Geochemistry Geophysics Geosystems, 15(3)

ISSN

1525-2027

Authors

Eilon, Zachary
Abers, Geoffrey A
Jin, Ge
et al.

Publication Date

2014-03-01

DOI

10.1002/2013gc005092

Peer reviewed

AGU PUBLICATIONS

Geochemistry, Geophysics, Geosystems

RESEARCH ARTICLE
10.1002/2013GC005092

Special Section:
Lithospheric Evolution of Cenozoic UHP Terranes: From Convergence to Extension

Anisotropy beneath a highly extended continental rift

Zachary Eilon[1], Geoffrey A. Abers[2], Ge Jin[1], and James B. Gaherty[2]

[1]Department of Earth and Environmental Sciences, Lamont-Doherty Earth Observatory of Columbia University, Palisades, New York, USA, [2]Lamont-Doherty Earth Observatory of Columbia University, Palisades, New York, USA

Abstract We have employed shear wave splitting techniques to image anisotropy beneath the D'Entrecasteaux Islands, in southeastern Papua New Guinea. Our results provide a detailed picture of the extending continent that lies immediately ahead of a propagating mid-ocean ridge tip; we image the transition from continental to oceanic extension. A dense shear wave splitting data set from a 2010 to 2011 passive-source seismic deployment is analyzed using single and multichannel methods. Splitting delay times of 1–1.5 s are observed and fast axes of anisotropy trending N-S, parallel to rifting direction, predominate the results. This trend is linked to lattice-preferred orientation of olivine, primarily in the shallow convecting mantle, driven by up to 200 km of N-S continental extension ahead of the westward-propagating Woodlark Rift. This pattern differs from several other continental rifts that evince rift-strike-parallel fast axes and is evident despite the complex recent tectonic history. We contend that across most of this rift, the unusually high rate and magnitude of extension has been sufficient to produce a regime change to a mid-ocean-ridge-like mantle fabric. Stations in the south of our array show more complex splitting that might be related to melt or to complex inherited structure at the edge of the extended region.

Key Points:
- *SK(K)S* splitting results from the Woodlark Rift, Papua New Guinea
- Majority of fast axes indicate spreading-parallel anisotropic fabric
- Quantitative link between shear in asthenospheric mantle and splitting magnitude

Supporting Information:
- README
- Figure S1–S10
- Table S1

Correspondence to:
Z. Eilon,
zeilon@ldeo.columbia.edu

Citation:
Eilon, Z., G. A. Abers, G. Jin, and J. B. Gaherty (2014), Anisotropy beneath a highly extended continental rift, *Geochem. Geophys. Geosyst.*, *15*, 545–564, doi:10.1002/2013GC005092.

Received 14 OCT 2013
Accepted 13 JAN 2014
Accepted article online 17 JAN 2014
Published online 1 MAR 2014

1. Introduction

The ability to constrain ongoing deformation and time-integrated stress fields makes shear wave splitting an ideal tool to interrogate dynamically evolving environments such as continental rifts. Several studies [*Gao et al*., 1997; *Kendall et al*., 2005] have applied shear wave splitting analysis to zones of active continental extension, or back-arc basins [e.g., *Smith et al*., 2001]. Most prior studies have focused on slow, intracontinental rifts that have undergone relatively little (up to a few tens of km) accumulated extension. By contrast, the Woodlark Rift in southeastern Papua New Guinea (Figure 1) exhibits the full range of extensional regimes, from ocean-floor spreading in the east to the first stages of continental thinning in the west, at rates reaching several cm/yr. The D'Entrecasteaux Islands (DI) lie on relatively thinned continental crust at the center of this continuum, immediately to the west of the youngest spreading centers. These islands are cored by topographic domes that expose ultrahigh pressure (UHP) metamorphic rocks at the surface, including the youngest-known coesite eclogite. Peak UHP metamorphism has been dated to 5–6 Ma [*Gordon et al*., 2012] or 7 Ma [*Zirakparvar et al*., 2011], implying average uplift rates of up to 20 km/Myr (based on pressure estimates from *Baldwin et al*. [2008]) coeval with 130–200 km of continental extension across these islands [*Taylor et al*., 1999]. Here, we use the term "continental crust" to mean nonoceanic, differentiated, metamorphosed crust, with thicknesses and seismic velocities characteristic of the continents, akin to terranes that have accreted to continents worldwide.

Several outstanding questions motivate investigation of this area. It is not clear how the unusually high rate and magnitude of extension is accommodated. Different mechanisms have been invoked to explain the exhumation of the UHP rocks, notably the end member models of Rayleigh-Taylor instabilities [*Ellis et al*., 2011; *Little et al*., 2011] and low-angle unroofing [*Hill et al*., 1992; *Webb et al*., 2008].

Shear wave splitting offers an understanding of time-integrated 3-D flow fields, thereby constraining mantle response to extension, as well as providing a sublithospheric framework for models of exhumation and extension. Several continental rifts (e.g., the Main Ethiopian Rift, MER [*Kendall et al*., 2005]) show significant seismic anisotropy (splitting times $\leq$2.5 s) with fast axes parallel to the strike of the rift. This is attributed to the strong anisotropic signal of melt within the lithosphere. In magma-poor rifts, where plate stretching accommodates extension, a spreading-parallel lithospheric fabric is expected [*Tommasi et al*., 1999], but this signal is likely to be weak due to trade-offs between strain and thickness. At mid-ocean ridges, by contrast,

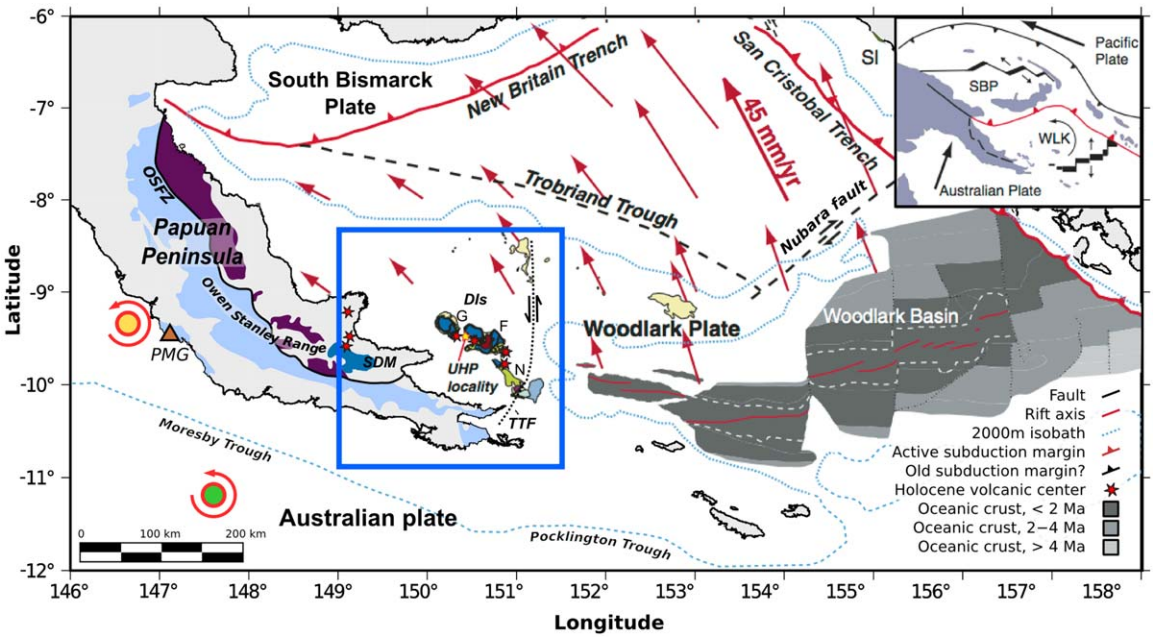

Figure 1. Tectonic map of southeastern Papua New Guinea [modified after *Baldwin et al*., 2008]. Euler poles for rotation of the Woodlark Plate (WLK) with respect to Australia (AUS) are shown: rotation about 6.0–0.5 Ma pole (yellow) at 4.02°/Myr (from *Taylor et al.* [1999] with correction to NUVEL-1A [*DeMets et al*., 1994]) preceded rotation about current pole (green) at 2.82°/Myr determined from GPS velocities [*Wallace et al*., 2004]. Current motions of WLK with respect to AUS according to best fitting block model [*Wallace et al*., 2004] are given by red arrows. Oceanic crust shown by gray shading, Brunes chron indicated by white dashed line, and recent shift in tectonics evident from the obliquity of present spreading ridges to magnetic isochrons. Purple shaded: PUB; light blue shaded: Owen-Stanley Metamorphics. DIs: D'Entrecasteaux Islands (G: Goodenough, F: Fergusson, N: Normanby); TTF: Trobriand Transfer Fault; OSFZ: Owen Stanley Fault Zone; SDM: Suckling-Dayman Massif. Blue box shows area of field deployment in later figures, active volcanic centers in this region only are depicted. Inset: simplified regional tectonics showing role of WLK and South Bismarck Plate (SBP) in mobile belt between obliquely converging Australian and Pacific (PAC) plates.

large splitting times are observed, with fast axes parallel to the spreading. This anisotropy arises from flow in the asthenospheric mantle that produces lattice-preferred orientation (LPO) of individually anisotropic crystals [e.g., *Blackman and Kendall*, 1997].

Our data provide the most detailed seismological information on the underlying structure of this region to date and our dense shear wave splitting data set contributes to the relatively few measurements of this sort from an extensional regime on the cusp between continental rifting and oceanic spreading. Our results imply that the unusually high strain rates and magnitudes of extension have created a strong unidirectional fabric at mantle depths that dominates any remnant structure from previous tectonism. This pattern differs from most other continental rifts, where extension and strains are much lower, suggesting that some critical strain has been reached whereby the mantle fabric aligns with flow.

2. Tectonic and Geologic Context

As many workers have detailed [*Pegler et al*., 1995; *Hill and Hall*, 2003; *Wallace et al*., 2004; *Baldwin et al*., 2012], Papua New Guinea is a unique natural laboratory for understanding tectonic processes. Since the Eocene, the tectonics have been controlled by the oblique convergence of the Pacific and Australian plates at ~110 mm/yr, accommodated by a broad deformational belt consisting of several microplates [*Tregoning et al*., 1998; *Wallace et al*., 2004]. In the late Miocene, the Woodlark microplate (WLK, which probably behaves as a rigid block together with the Solomon Sea plate [*Wallace et al*., 2004]) began rotating away from the Australian continent (AUS); driven by slab pull at the northern boundary of the Solomon Sea [*Weissel et al*., 1982; *Wallace et al*., 2004].

Taylor et al. [1999; *Goodliffe and Taylor*, 2007] used magnetic anomalies in the Woodlark Rift east of 152°E to describe the relative WLK-AUS motion since ~8.4 Ma as anticlockwise rotation about an Euler pole at (9.3°S, 147°E) at −4.022°/Myr. New seafloor has been produced diachronously at westward propagating spreading centers since 4–6 Ma and the DI lie just west of the rift tip (151.7°E), along the extrapolated line of the youngest spreading center. Seismic tomography shows an abrupt transition from slow continental crust to

fast oceanic crust to the immediate east of the DI [*Ferris et al*., 2006]. GPS data show that the current relative motion between the Trobriand Block and AUS is −2.74°/Myr about a pole at (9.43°S, 147.5°E) [*Wallace et al*., 2012]. The difference in poles results in a ∼30% discrepancy between long-term geologic rates of divergence (∼30 mm/yr) and geodetic rates (∼15–20 mm/yr) across the DI [*Wallace et al*., 2012] possibly due to a tectonic rearrangement at ∼0.52 Ma [*Taylor et al*., 1999].

Simple calculations using the geologic poles require ∼190 km of extension somewhere at the longitude of Normanby Island (151°E) and ∼140 km across Goodenough Island (150°E) [consistent with *Kington and Goodliffe*, 2008] (Figure 2). However, the absence of obvious structures that have accommodated this divergence has led to concern over whether the whole WLK block is deforming rigidly at rates predicted by the seafloor anomalies. Left-lateral slip on the Nubara fault (which at present has a right-lateral sense) or significant displacement on the Trobriand Transfer fault [*Little et al*., 2007] could decouple the DI from the seafloor to the east, making the above estimates of extension upper bounds, although there is little evidence of

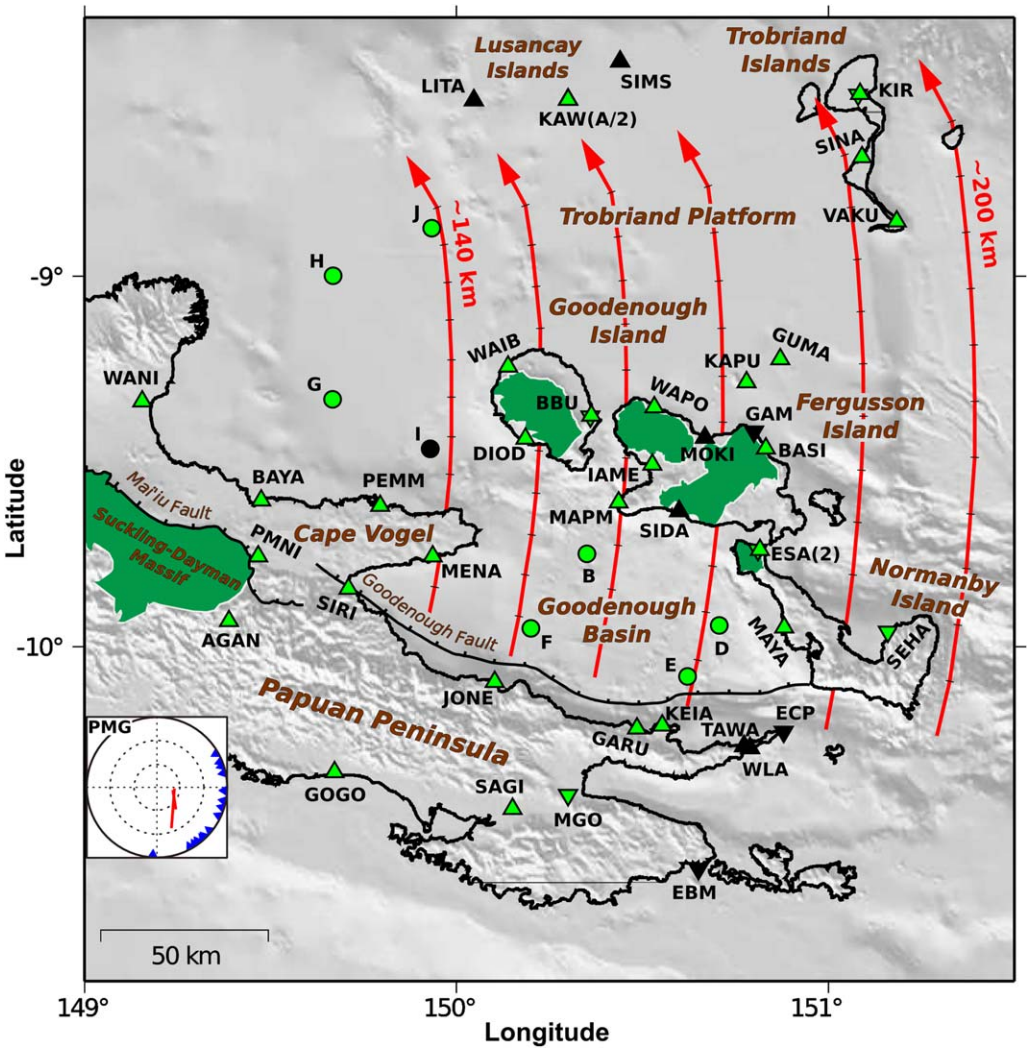

Figure 2. Map showing deployment of broadband seismic stations. Green symbols indicate stations for which shear wave splitting results were obtained, black symbols are stations with no splitting results. Circles are ocean bottom seismometers, point-upward triangles are land stations in this experiment, inverted triangles are stations that were occupied during the 1999–2000 Woodseis experiment (overlapping triangles therefore denote reoccupied sites, BBU, ESA, and KIR); gneiss domes/metamorphic core complexes indicated in green; red arrows indicate cumulative vectorial extension calculated over the last 6 Ma, accounting for the changes in rate/pole at 500 kyr and 80 kyr and tick marks indicate 0.5 Myr intervals. Recent GPS results indicate that approximately 10 mm/yr of extension is taking place on structures within Goodenough Basin and the northern coast of the D'Entrecasteaux Islands is moving northward away from stable Australia at an additional 15 mm/yr [*Wallace et al*., 2012]. Inset: shear wave splitting results from the Port Moresby GSN station, plotted at lower-hemisphere pierce points. Blue triangles indicate back azimuth of good quality null measurements; red lines indicate measured splitting (cf. Figure 7).

large offset on the Trobriand platform where a Trobriand strike-slip fault has been postulated [e.g., *Goodliffe et al*., 1999]. Extension around the DI and within the Papuan Peninsula is connoted by ongoing tectonism, including low-angle normal-faulting earthquakes [*Abers et al*., 1997] on structures that follow steep scarps bounding the islands. Raised terraces along the north coast of the Papuan Peninsula, as well as fluvial incision profiles, confirm that extension is currently accommodated on the Goodenough and Mai'iu fault structures (Figure 2) in concert with exhumation of the Suckling-Dayman Massif [*Mann et al*., 2009; *Miller et al*., 2012].

The DI include several topographically dominant gneiss domes [*Ollier and Pain*, 1980], often called metamorphic core complexes (MCCs) [*Davies and Warren*, 1988], which contain the youngest-known UHP metamorphic rocks [*Baldwin et al*., 2004]. The mechanism for dome exhumation is beyond the scope of this paper but there is consensus that it is tied to tectonic extension [e.g., *Webb et al*., 2008; *Ellis et al*., 2011]. These domes are bounded by numerous faults and mylonitized shear zones and are intruded by plutons. Recently, workers have argued that there is a radial pattern to microstructural lineations in the carapace, inferred to represent diapiric exhumation [*Little et al*., 2011]. Exhumation time scales for these domes are constrained by CA-TIMS dating, which yielded ages of 5.82 $\pm$ 0.20 Ma to 4.78 $\pm$ 0.17 Ma [*Gordon et al*., 2012] or 7.1 $\pm$ 0.7 Ma [*Zirakparvar et al*., 2011] for a coesite-bearing eclogite that has since ascended $>$100 km, and put the earliest intrusions at 3.49 $\pm$ 0.01 Ma [*Gordon et al*., 2012]. Clastic sediments in the Trobriand basin sediments to the north indicate that the domes broke sea level $\sim$3 Ma [*Francis et al*., 1987], while raised coral reefs and stream-profile modeling [*Miller et al*., 2012], demonstrate ongoing uplift of these edifices since mid-Pliocene to their present elevations of $\leq$2.5 km.

Abers et al. [2002] used teleseismic *P* wave (Vp) tomography to show a broad low-velocity region beneath the DI and extending some distance beneath the Woodlark Basin. The Vp anomalies are up to 5% slow within the upper mantle and indicate significant lithospheric thinning in a swath from the westernmost spreading center to Normanby Island. Associated upwelling and melting is represented by widespread intrusive and extrusive igneous activity; the DI contain Pliocene-Pleistocene granodiorite intrusions and Quaternary calk-alkaline extrusive volcanism, with variably deformed leucosome dikes crosscutting the domes [*Gordon et al*., 2012]. Historically active volcanic stratovolcanoes lie in a rough E-W line along strike from the present-day spreading centers, and include Mt. Victory and Goropu on the Papuan mainland, and the Walilagi Cones, Iamelele, and the Dawson Strait group on the D'Entrecasteaux themselves. The lavas produced at these volcanic centers have geochemical signatures indicative of a subduction-enriched melt source region, including Ba/La ratios greater than 20 and LREE enrichment [*Smith and Johnson*, 1981]. The Trobriand arc and the geochemistry suggest that subduction may have been important to recent dynamics, although the eastern volcanics trend to more alkalic compositions with a more rift-like character [*Stolz et al*., 1993]. *Abers et al*. [2002] found no evidence for a subducted plate, and a regional tomography study clearly imaging fast New Britain and Solomon slabs shows no fast anomaly associated with the Trobriand arc [*Hall and Spakman*, 2002].

3. Data and Methods

3.1. Deployment and Data

We installed an array of land and ocean-bottom broadband seismic stations over a $\sim$250 $\times$ 250 km area just west of the propagating rift tip, approximately centered on the DI (Figure 2). The seismic deployment comprised 8 ocean-bottom broadband seismographs (Trillium 240 with 240s-corner seismometers, with differential pressure gauges not used in this analysis) and 31 land-based PASSCAL broadband instruments (Guralp CMG-3T with 120s-corner sensors) that were installed by direct burial. Orientations of all stations were checked (see section 3.2) and corrections made where necessary. All instruments recorded at 50 sps, and we did not decimate for the splitting analysis. The array operated variously between March 2010 and late July 2011, with 86% data recovery, including retrieval of all 8 OBS instruments in January 2011. Several stations had intermittent power problems, and broadband seismic channels for OBS "I" failed, but most stations had sufficient data for splitting analysis. We also used data from several of the stations deployed during the 1999–2000 Woodseis experiment [*Abers et al*., 2002; *Ferris et al*., 2006].

3.2. Station Orientation

For the purposes of shear wave splitting, it is essential to know the sensor orientation accurately. Ocean-bottom seismometer (OBS) instruments are self-leveling but the azimuths of the horizontal channels

depend on how the instrument descends to the seafloor. We determined the orientations of our broadband OBS stations using Rayleigh wave polarization across several teleseismic events [*Stachnik et al*., 2012], specifically by maximizing the cross correlation at zero lag between the Hilbert transform of the vertical component (to correct for the -90° phase shift involved in the elliptical retrograde particle motion) and the resolved radial component [*Baker and Stevens*, 2004]. We ascertained correction angles for all seven functioning OBS instruments with confidence bounds (on average $\pm 5^\circ$) produced using a nonparametric linear bootstrap, with the balanced resampling method. These uncertainties may be compared favorably to the average uncertainty in land-based station orientation and are on the order of variation in arrival azimuth due to scattering/diffraction along the raypath. Four land stations were also found to have $\sim$10 to 20° misalignments, probably due to erroneous declination corrections during installation, and were corrected (see supporting information).

3.3. Single-Channel Splitting Methods

For the shear wave splitting analysis, we used earthquakes with $M_w \geq 6.25$ within the relevant *SK(K)S* distance window ($\sim$85° to $\sim$140°), giving a total of 21 earthquakes. The back-azimuthal distribution of these earthquakes was highly nonuniform, dominated by events from the Andean margin in 2010 (Figure 3).

The SplitLab software package [*Wüstefeld et al*., 2008] was used to make individual shear wave measurements, using a band-pass filter of 8–50 s and manually picked windows ($\sim$15–25 s long) around the shear-wave arrivals. Measurement quality was manually designated "good," "fair," or "poor" on a case-by-case basis, based on signal-to-noise ratio (SNR), minimal associated energy on the vertical component, impulsivity of arrival, minimal energy on horizontal components before the predicted arrival, and small estimated errors in splitting parameters, following standard practice [e.g., *Long et al*., 2010]. We discarded traces with SNR < 3, arrivals for which the cross correlation between the transverse and the time derivative of the radial was less than 0.6 [following e.g., *Chevrot*, 2000], and likely null measurements for which the estimated fast azimuth was closer than 15° to the measured polarization. We inverted the seismograms for the two splitting parameters, fast azimuth (φ) and time delay (δt), by grid searching through model parameter space for $-90 < \varphi \leq 90^\circ$ and $0 \leq \delta t \leq 4$ s, seeking the solution that minimized energy on the corrected transverse component (the SC method, after *Silver and Chan* [1991]) (Figure 4). We prefer this method based on tests of several shear wave splitting methods (section 3.6 and supporting information).

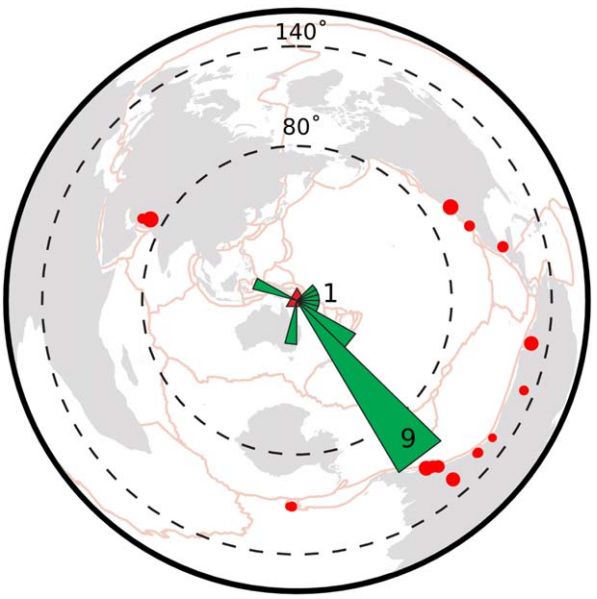

Figure 3. Earthquake data set used for *SK(K)S* splitting with the single channel method. This catalog comprises earthquakes larger than M_w 6.25, that took place between 4 March 2010 and 20 June 2011, in the distance range from 85 to 140° from the center of the array.

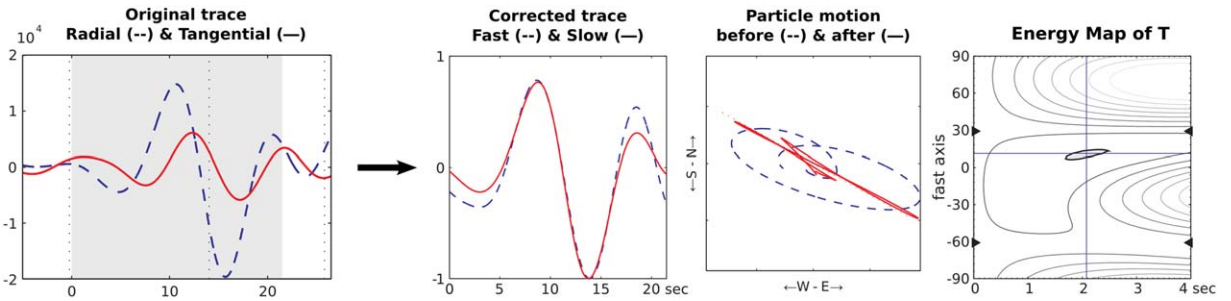

Figure 4. SC measurement for a SKS arrival at station BAYA, on the north coast of Cape Vogel, from a M_w 7.2 earthquake was 91° away from the station. Thin lines are 12.5% energy contours spaced evenly between the maximum and minimum, and the shaded region is the 95% confidence region for the energy minimum. The signal had a measured SNR of 16.7 and the traces were band-pass filtered from 8 to 50 s. The linearized particle motion and near-identical fast/slow waveforms indicates well-resolved splitting. This measurement was designated "good" quality (section 3.3).

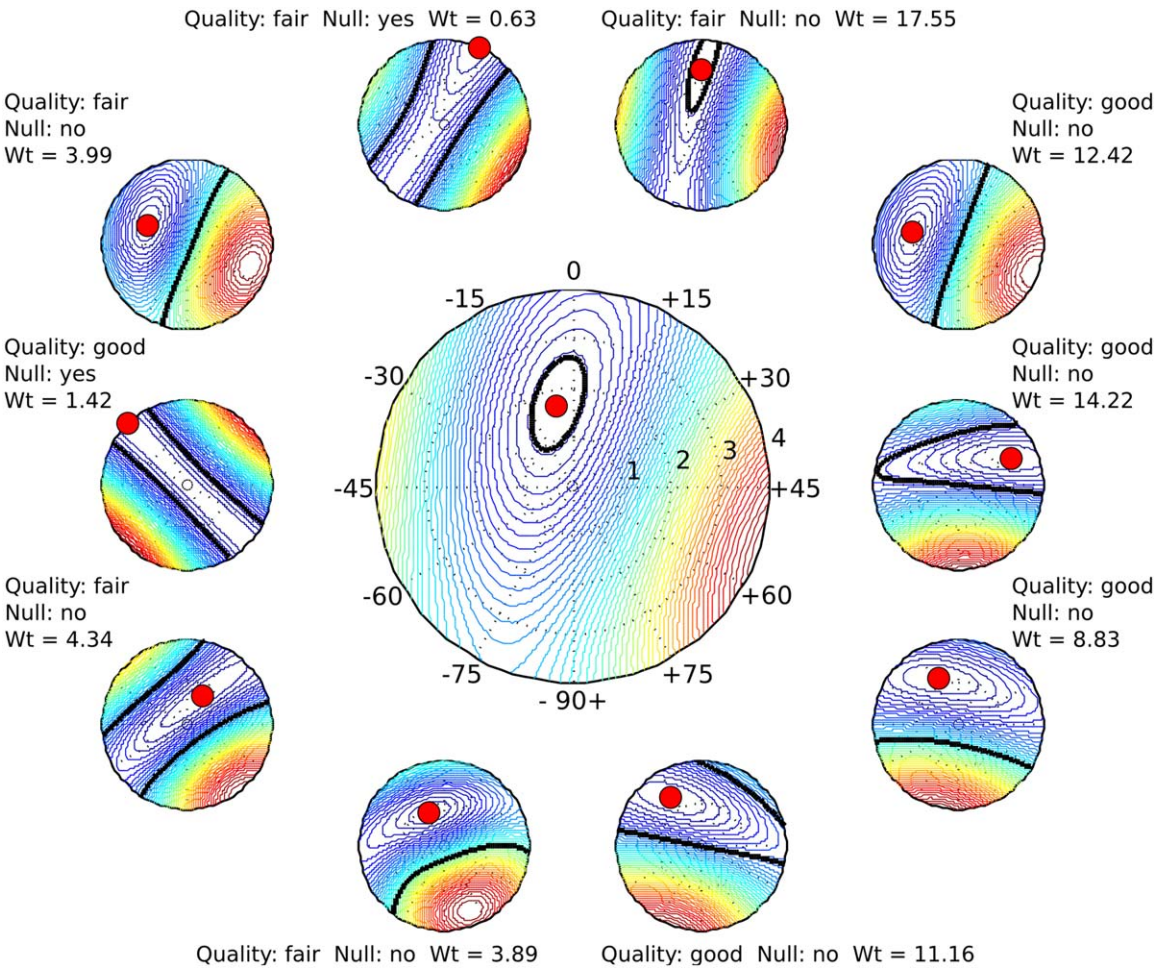

Figure 5. Stacked splitting result at station PEMM, with contoured energy surfaces for each individual arrival (peripheral) and the stack (central) from the minimum energy (SC) method [*Silver and Chan*, 1991]. Relative energy for each plot is shown by 2% contours, scaled to the energy range separately for each plot, and colored from high energy (red) to low energy (blue). Best fit: $dt = 1.68$ s $\pm$ 0.72 s and $\varphi = -4.0° \pm 8.0°$ (2σ errors). Weights (Wt) of individual measurements in the stack are calculated as the product of the measured SNR [after *Restivo and Helffrich*, 1999] and the quality (1 for fair, 2 for good). Splitting parameter measurements are made at the energy minima (red dots), where splitting time (0–4 s) is indicated by radial distance and fast axis by angle (0–360°). 95% error bounds are shown by thick black lines, calculated according to the method of *Silver and Chan* [1991]. Note that the splitting model parameters are evenly spaced in φ and δt so these are conic projections.

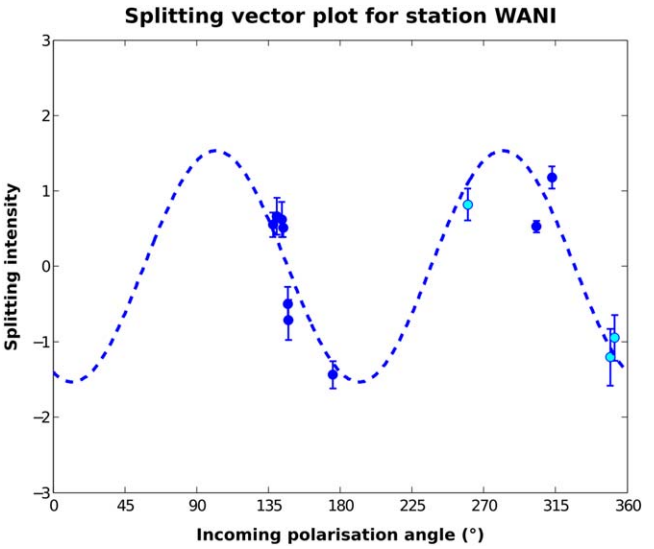

Figure 6. SI results (with 2σ error bars) for station WANI. The least squares $\sin(2\theta)$ fit to the splitting vector gave splitting parameters of $\varphi = 57.0^\circ$, $\delta t = 1.53$ s, $Erms = 0.17$. The calculated F statistic for this fit is 18.95, giving a negligible chance that the fit is not statistically better than null. Blue symbols: *SK(K)S* arrivals, cyan symbols: direct *S* arrivals from deep focus (>450 km) earthquakes.

3.4. Stacking of Individual Measurements

We stacked weighted error surfaces over individual measurements, where possible, to improve the robustness of the splitting measurement at each station [*Wolfe and Silver*, 1998] (Figure 5). Picks with qualities of "good," "fair," and "poor' were given weights of 2, 1, and 0, respectively, and weights were multiplied by the measured SNR [*Restivo and Helffrich*, 1999] based on synthetic tests which showed that fidelity of estimated model parameters to "true" inputs increased with SNR (see supporting information). Null measurements were included in the stacks with weights scaled down to 10%, to prevent deep minima in null energy surfaces from dominating the stacks. Uncertainties were calculated assuming the errors are χ^2 distributed and using the inverse F distribution to find 2σ bounds, with estimates of the degrees of freedom calculated for each trace using the first zero crossing of the autocorrelation function [*Yang et al.*, 1995].

3.5. Multichannel Method

To complement the individual results, we use the approach of *Chevrot* [2000], which measures anisotropy beneath each station in different sense. This method relies upon the predicted 180° periodicity (a "2θ" pattern) in the back-azimuthal variation of splitting intensity (SI), defined as $s = -2Tr/|r|^2$ where $r = dR/dt$, the time derivative of the radial component, and T is the transverse component seismogram (Figure 6). The success and reliability of this technique depends on a wide back-azimuthal distribution and so we augmented the *SK(K)S* data, described above, with direct *S* arrivals (from 40 to 80°), using only those from deep (>450 km) source events in an attempt to minimize the influence of source-side splitting [e.g., *Fouch and Fischer*, 1996]. This added three earthquakes to our data set that had clear *S* arrivals. We calculated the polarization of direct *S* arrivals by stacking horizontal components across the array and taking the inverse cosine of the first eigenvector of the 2-D covariance matrix [*Vidale*, 1986]. Arrivals were discarded if measured polarization was too dissimilar (>15°) to the CMT solution prediction or if (for nonnulls) the cross correlation between the transverse and the time derivative of the radial was less than 0.7. Although *Foley and Long* [2011] noted significant source-side splitting from deep events in the Tonga slab, our deep-source direct *S* measurements agreed well with the *SK(K)S* results, so were retained. Splitting parameters were calculated using a weighted least-squares fit to the splitting intensity, weighting by the formal uncertainties [*Chevrot*, 2000] of the measurements.

3.6. Method Comparison

Some authors [e.g., *Long and Van Der Hilst*, 2005; *Vecsey et al.*, 2008] have sought to qualitatively compare the performance of the three principal individual-arrival methods (rotation-correlation [e.g., *Bowman and Ando*, 1987], the minimum energy method used here [*Silver and Chan*, 1991], and eigenvalue minimization [e.g., *Silver and Chan*, 1991]) for measuring shear wave splitting. In terms of consistency, reliability, and robustness (see supporting information) we prefer the SC method of the single-channel techniques, in agreement with *Vecsey et al.* [2008]. In the case of simple structure, we find that the SI method is extremely successful (although it overestimates splitting times in some cases) but note that this technique obscures some of the hallmarks of complicated structure at depth [cf. *Silver and Long*, 2011].

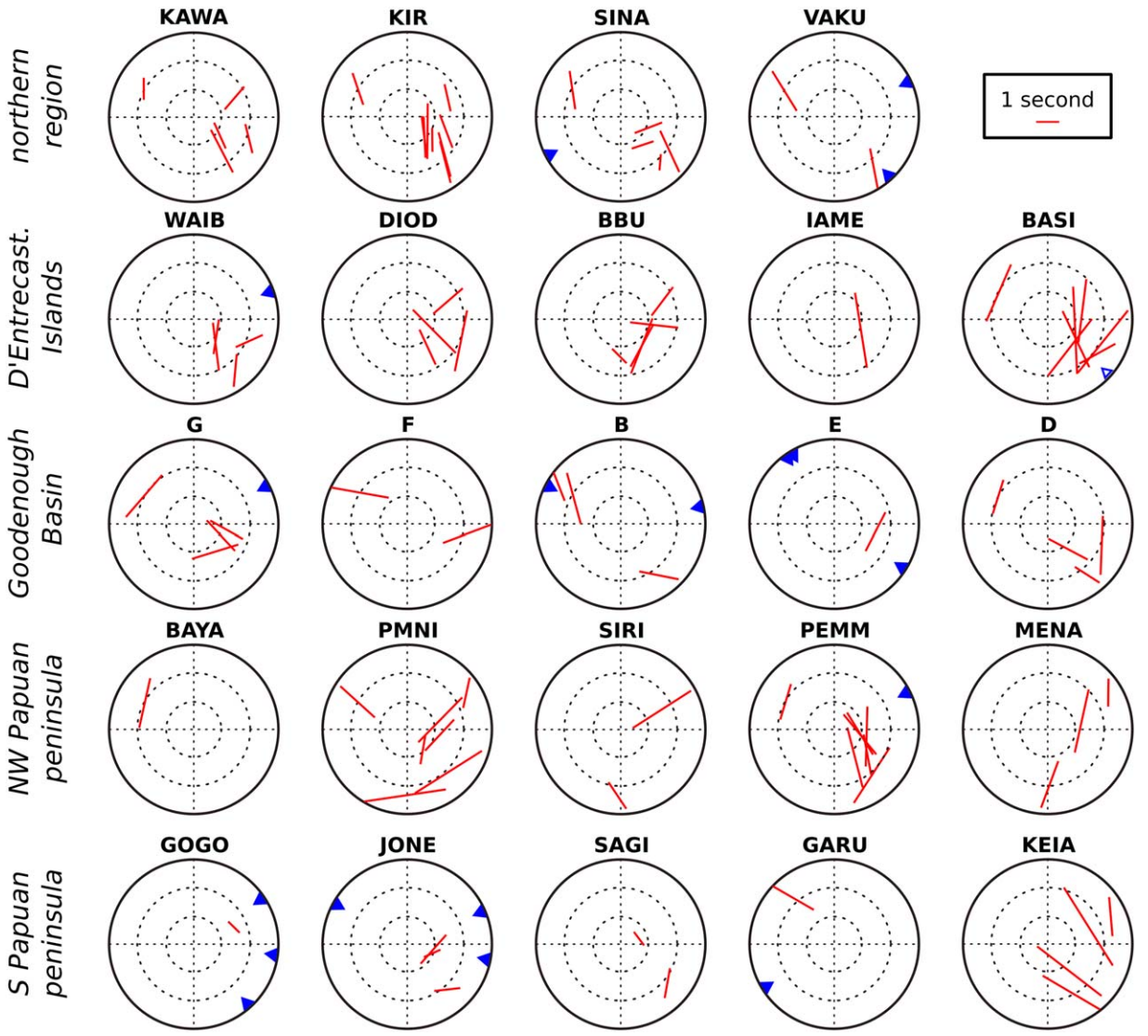

Figure 7. Individual splitting results at representative stations, from five broad regions (indicated at left), where length and orientation of lines indicate δt and φ, respectively. Results are plotted according to incident angle (angles of 15°, 10°, and 5° shown by concentric circles) and back azimuth, using a lower-hemisphere projection, and only "good" and "fair" nonnull results are shown. Blue triangles indicate measured polarization of "good" null results.

4. Results

4.1. Single-Channel Methods

Splitting parameters were estimated for *SK(K)S* arrivals at each station. Following the results of our synthetic tests, we use results from our preferred method (SC) that meet criteria defined in section 3.3. We obtained results from the majority of our stations, including all seven functioning OBS. Figure 7 shows individual measurements from a representative selection of stations across the array. The results of one station stack (see section 3.4) are shown in Figure 5 where polar projections display how individual measurements contribute to the stack. All stacked results from the SC method are shown in Figure 8, and full results are given in Table 1. An analysis of frequency dependency at stations KIR and AGAN showed no significant difference in splitting for band-pass filters of 1–5 s, 5–10 s, and 10–100 s period, although splitting measurements were much poorer for the highest-frequency inputs.

The splitting in the north and on the DI is clear, with fast directions approximately north-south and splitting times on the order of 1–1.5 s (Figure 8). Importantly, this observation is consistent across arrival, back azimuth, and station, indicating that a simple fabric pervades the northern region of our array. This region was

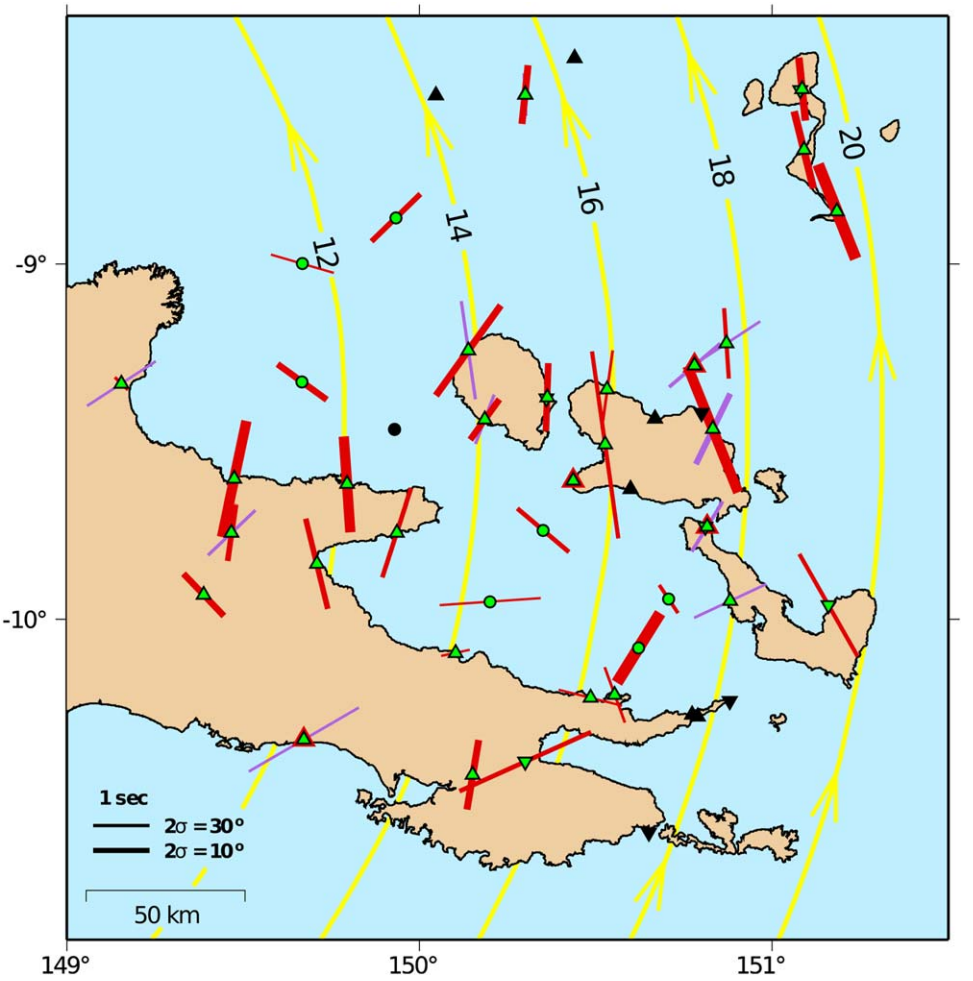

Figure 8. Stacked splitting results from the SC method (red) and SI method (magenta), where the orientation of the lines indicates the azimuth of measured fast axes and their length is the associated time delay. Line thickness corresponds to the uncertainty in the fast azimuth; we emphasize less uncertain measurements with thicker lines (see key). For the SC results, formal uncertainties in splitting parameters are estimated from the energy surface (section 3.4), while for the SI results we use a bootstrap—see Supporting Information Table S1 for numerical values. Stations with only null SC results are circled in red. Yellow lines are small circles about best fitting WLK-AUS pole derived from GPS data [*Wallace et al.*, 2012] with present-day rates (in mm/yr) relative to AUS indicated. Station symbols are the same as Figure 2.

also characterized by agreement between results of the three single-channel methods, which is a good indicator of simple structure [*Long and Van Der Hilst*, 2005].

The individual measurements in Goodenough Basin and the southeastern Papuan Peninsula are more complex, particularly a broad swath running approximately parallel to the rift axis to the south of the D'Entrecasteaux. We observe rapidly varying or contradictory splitting between stations and between different arrivals at a given station. Several stations (e.g., B, D, G) exhibit two populations of measured fast axes, depending on back azimuth, some trending approximately N-S and others trending ENE-WSW, parallel to the rift zone. Station stacks within this region show large ($\leq$90°) changes in direction of apparent fast axis between nearby stations. Interestingly, the three single-channel methods return similar results in this region (see supporting information Figure S7), which is not normally the case for complex anisotropy [*Levin et al.*, 2004; *Long and Silver*, 2009].

Most of these apparently anomalous measurements have high SNR and clear minima in the error surfaces. Although many of the anomalous results are measured at the OBS sites, which traditionally have low SNR on the horizontal channels used for shear wave splitting [*Webb*, 1998], we consider these measurements to be fairly robust given the good quality of the arrival waveforms and the fact that some of the adjacent land stations (e.g., KEIA, MAYA) show similar results. The OBS's all lie in enclosed, isolated basins, so the long-

Table 1. Splitting Results for All[a] Stations[b]

Station	avSNR	dof	*N*(null)	dtSC	phiSC	Nsim	dtSI	phiSI
AGAN	7.56	126	9(6)	1.0 ± 0.3 s	−44 ± 8			
BASI	8.12	116	8(5)	2.4 ± 0.4 s	−22 ± 3	13	1.4 ± 0.2 s	26 ± 6
BAYA	16.72	9	1(0)	2.1 ± 0.4 s	12 ± 3			
BBU	11.81	63	5(1)	1.2 ± 0.2 s	2 ± 8			
DIOD	8.39	98	7(3)	0.9 ± 0.1 s	36 ± 8	11	0.9 ± 0.4 s	21 ± 29
ESA2	9.33	115	7(7)	0.1 ± 0.1 s	32 ± 38	5	1.0 ± 2.1 s	32 ± 18
GARU	11.23	26	2(1)	1.2 ± 0.6 s	−76 ± 89			
GOGO	10.09	82	6(5)	0.2 ± 0.2 s	−58 ± 48	7	2.3 ± 1.7 s	60 ± 52
GUMA	8.08	62	4(3)	1.2 ± 0.4 s	−4 ± 17	12	1.4 ± 0.9 s	57 ± 47
IAME	3.85	10	1(0)	3.3 ± 1.2 s	−8 ± 18			
JONE	6.05	69	5(0)	0.5 ± 0.3 s	78 ± 89			
KAPU	10.45	54	4(4)	0.6 ± 0.3 s	−46 ± 8	12	1.2 ± 0.8 s	50 ± 19
KAWA	10.08	54	4(0)	1.0 ± 0.2 s	6 ± 7	10	0.8 ± 2.3 s	357 ± 38
KEIA	7.13	41	3(0)	1.0 ± 1.4 s	−20 ± 48			
KIR	7.06	106	9(0)	1.1 ± 0.1 s	−6 ± 6	13	0.6 ± 0.8 s	4 ± 34
MAPM	5.73	28	2(2)	3.0 ± 1.0 s	−50 ± 3			
MAYA	10.50	85	6(4)	0.4 ± 0.4 s	52 ± 16	11	1.4 ± 0.8 s	65 ± 39
MENA	5.19	34	3(1)	1.6 ± 0.6 s	18 ± 15			
PEMM	6.65	116	10(2)	1.7 ± 0.3 s	−4 ± 3			
PMNI	9.17	88	7(3)	1.0 ± 0.2 s	8 ± 10	13	1.2 ± 0.6 s	47 ± 26
SAGI	7.63	29	2(1)	1.2 ± 0.2 s	10 ± 7			
SEHA	5.21	15	1(0)	2.1 ± 1.3 s	−30 ± 17			
SINA	8.49	71	6(1)	1.4 ± 0.2 s	−14 ± 6			
SIRI	11.02	19	2(0)	1.6 ± 1.1 s	−14 ± 10			
VAKU	5.89	132	9(7)	1.8 ± 0.4 s	−22 ± 2			
WAIB	9.40	61	5(2)	2.0 ± 0.7 s	36 ± 7	9	1.7 ± 1.3 s	352 ± 32
WANI	12.41	63	4(3)	0.3 ± 0.1 s	−46 ± 30	12	1.5 ± 0.5 s	58 ± 40
WAPO	4.56	14	1(0)	1.4 ± 1.7 s	8 ± 47			
B	6.40	72	6(4)	1.2 ± 0.8 s	−50 ± 14			
D	7.48	56	5(2)	0.6 ± 0.3 s	−34 ± 28			
E	11.45	43	4(3)	1.4 ± 0.3 s	32 ± 2			
F	6.91	11	2(0)	1.8 ± 1.1 s	86 ± 89			
G	10.07	55	5(1)	1.1 ± 0.4 s	−54 ± 8			
H	5.76	46	3(0)	1.2 ± 0.4 s	−74 ± 89			
J	7.15	19	2(0)	1.2 ± 0.5 s	46 ± 10			

[a]Note only stations with at least one single channel measurement that passed quality control criteria (see section 3.3) are shown.

[b]Columns are: (1) station name; (2) average SNR within time windows used for the SC method; (3) total degrees of freedom after stacking; (4) the number of measurements in the SC stack, with the number that were null in brackets; (5) estimated splitting time of the stacked SC result, in seconds, $\pm 2\sigma$; (6) estimated fast azimuth of the stacked SC result, $\pm 2\sigma$; (7) number of splitting intensity measurements used in the SI method calculation; (8) estimated splitting time using the SI method, in seconds, $\pm 2\sigma$; and (9) estimated fast azimuth using the SI method, $\pm 2\sigma$. For the SI method, errors were estimated using the balanced resampling bootstrap method, and a weighted L2 fit. Few stations had good SI measurements.

period tilt noise commonly associated with infragravity waves may be low compared with more typical open-ocean sites [e.g., *Webb and Crawford*, 2010].

In the northeastern Papuan Peninsula, stations in the northwest near Cape Vogel evince fast directions approximately north-south. This appears to be a continuation of the structure on the DI. A Rayleigh wave phase velocity map calculated at 32 s period (Figure 9) shows a continuous region of low velocities beneath the DI extending westward beneath Cape Vogel, at least as far west as 149°E [*Jin et al.*, 2013]. Surface waves of this period are sensitive to the uppermost mantle, and we attribute this low-velocity region to elevated temperatures along the axis of the rift where the lithosphere has been thinned. This result supports previous evidence that lithospheric thinning within this rift is localized to the axis [*Abers et al.*, 2002]. The low-velocity swath also coincides with locations of recent volcanism [*Smith and Milsom*, 1984]. We observe strong (>1 s) splitting, at stations overlying the region of slow phase velocities, and consistently rift-perpendicular fast axes.

Results from PEMM and MENA, on Cape Vogel itself, showed significant discrepancies between the different single-channel splitting methods. Stations further to the east and on the southern coast of the Papuan Peninsula generally returned very few splitting results. While some of these were noisy stations, several results from GOGO, a good station on the southern coast, were null measurements. This might be a happenstance of the incident polarizations, or it might imply that the magnitude of the coherent anisotropy decreases going southeastward across the peninsula (section 5.1.4). For reference, we analyzed splitting at the Port

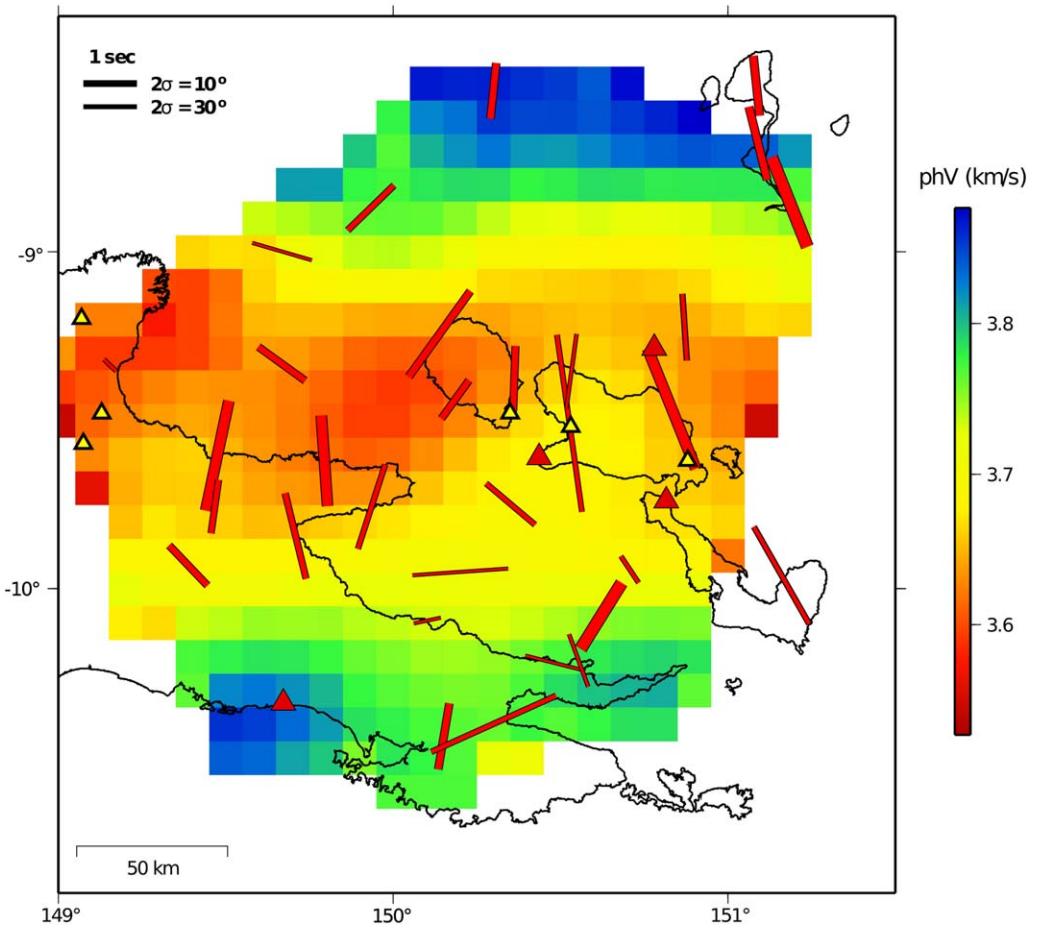

Figure 9. Splitting results from the SC method only (red lines) superimposed on results from a 3-D phase velocity (phV) inversion using Rayleigh wave signals from ambient noise and teleseismic earthquakes [*Jin et al.*, 2013]. The mean phase velocity at this period was 3.71 km/s. Yellow triangles correspond to volcanoes that have been active in the Quaternary. Line thickness, length, and orientation as in Figure 8; red triangles are stations dominated by null splitting measurements.

Moresby global seismic network station (PMG), about 200 km to the west of our field area, and found that the overwhelming majority of arrivals at this station are clear nulls (Figure 2).

4.2. SI Method

The SI method requires several shear-wave arrivals to produce a measurement and so yielded results from fewer stations than the single-channel methods, even with the added direct *S* arrivals. We show only results that are obtained by fit to at least five splitting intensity measurements. Using an *F* test, we show that only six of the station measurements fit the observed splitting intensities significantly (at $p = 5\%$) better than a null hypothesis of no splitting. Despite this, many of the results with less statistically significant fits are consistent with the more robust SI results so in Figure 8 we include the 12 results that give a better fit than null at $p = 33\%$ (1σ).

The SI observations indicate that structure in the north, beneath the DI and Trobriand Islands is ~NNE-SSW, consistent with SC method results. On Cape Vogel, whereas the φ_{SC}'s align roughly N-S, the φ_{SI}'s trend NE-SW. This ~45° disagreement between the two methods might imply complex structure, or it may be that the SI results are being dominated by the (often noisy) arrivals from a back azimuth of ~140°. Arrivals with anomalously energetic transverse components from one azimuth will produce large splitting intensities that force the $2-\theta$ sinusoid to fit a peak at that azimuth. To explore this possibility we also fitted the splitting vector using the L1 norm, which is less weighted toward outliers, and obtained almost identical φ's with marginally smaller (by 0.1–0.2 s) δt's.

The splitting magnitudes estimated by the SI method are on the order of 1 s, which qualitatively agrees with single channel methods. Discrepancies of ~0.5 s between δt_{SI} and δt_{SC} are probably not significant,

given similar uncertainties in δt_{SI} indicated by synthetic tests (supporting information Figure S6d). Measurements of φ at individual stations differ between the SI and SC methods by an average of 21 $\pm$ 13°, not including the two stations with significant discrepancies, GOGO and WANI. These two stations have unclear or null SC results, but $\delta t_{SI} \approx$ 1–1.5 s, $\varphi_{SI} \approx$ 40–60°.

5. Discussion

5.1. Anisotropy Beneath the D'Entrecasteaux

5.1.1. A Simple, Extension-Related Fabric

SK(K)S shear wave splitting indicates seismic anisotropy somewhere on the receiver side of the raypath beneath a station. Our splitting results overwhelmingly indicate N-S trending azimuthal anisotropy beneath this region. At stations on the Papuan Peninsula north of ~10°S as well as on the DI and the northern islands, N-S splitting is observed across different phases and polarizations, and splitting analyses using different methods produce consistent results (Figure 8 and supporting information). Such coherency of measurements makes a strong case for simple, horizontal seismic anisotropy beneath the northern two-thirds of our array, probably in the upper mantle [*Long and Van Der Hilst*, 2005; *Long and Silver*, 2009].

Anisotropy is commonly attributed to lattice-preferred orientation (LPO) of individually anisotropic mineral grains, whereby bulk alignment evolves as a response to finite strain [*Christensen*, 1984]. The fast axis of anisotropy in olivine-dominated mantle is widely observed to align with inferred mantle flow direction [*Soedjatmiko and Christensen*, 2000; *Gaboret et al*., 2003; *Becker et al*., 2008], in agreement with experimental and xenolith data for olivine deforming by dislocation creep from a wide range of P, T, f_{O_2} conditions [e.g., *Ismaïl*

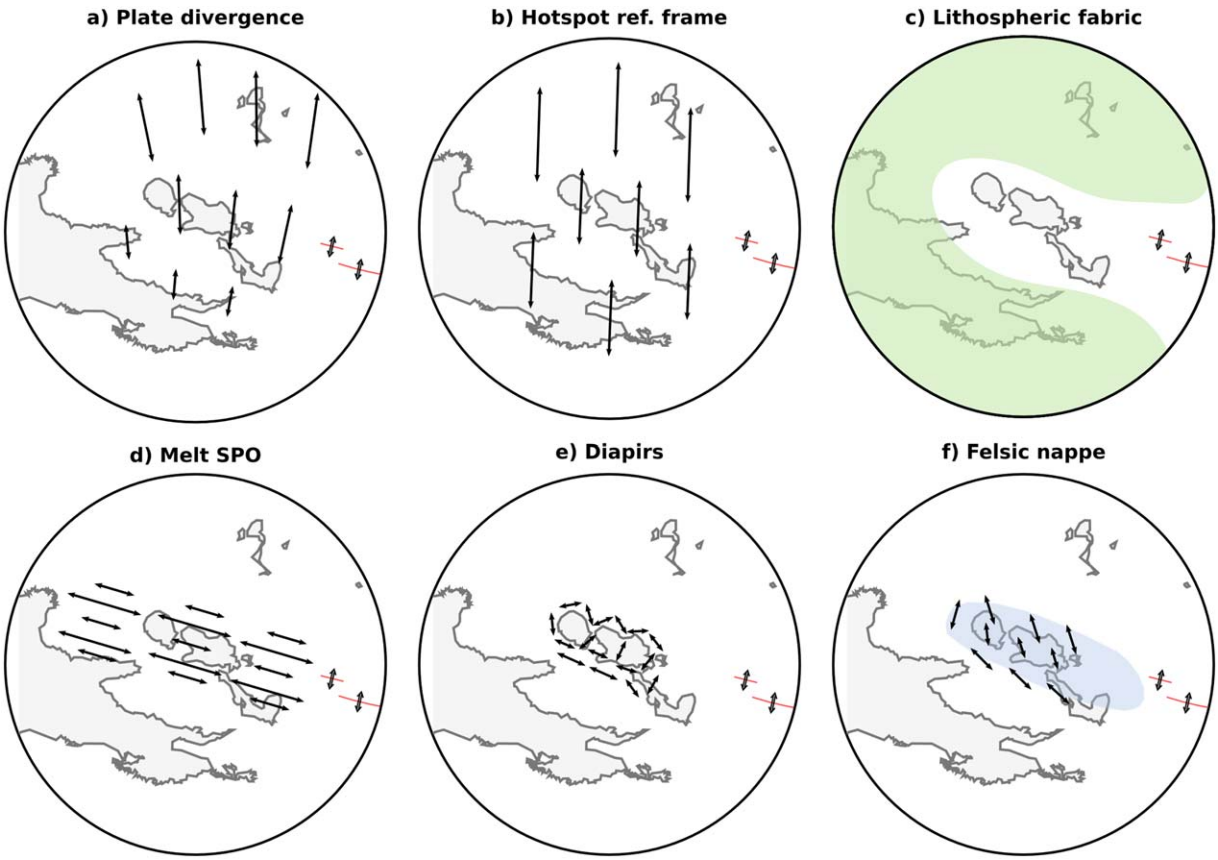

Figure 10. Cartoons depicting various possible contributions to the anisotropy; arrows qualitatively indicate predicted magnitude of δt and azimuth of φ. Putative rift axis given by red lines. (a) Anisotropy from LPO due to shear between the shallow convecting mantle and plates moving in the hot spot reference frame. (b) Anisotropy (fabric unknown, extent indicated by green shading) frozen into lithosphere would be expected to vary with lithospheric thickness. (c) Anisotropy expected from aligned melt pockets at axis of rifting and volcanism, cf. Ethiopia Rift. (d) Anisotropy due to radial perturbations to mantle flow field around diapirs implicated in formation of gneiss domes [e.g., *Little et al*., 2011]. (e) Anisotropy due to superposition of westwards along-axis flow of diapiric material (blue shading) and axis-normal corner flow [after *Ellis et al*., 2011]. (f) Anisotropy due to shearing beneath diverging plates, here depicted as asymmetric. The majority of our splitting measurements agree with predictions for plate divergence, except in the south.

and Mainprice, 1998; *Tommasi et al*., 2000; *Blackman et al*., 2002]. Thus, the anisotropic structure observed in our field region suggests a dominant component of N-S flow or distributed shearing in the mantle related to the N-S extension. Despite the youth of this extensional regime, the rate and magnitude of the divergence have been sufficient to establish a strong flow-parallel LPO that dominates the anisotropy.

While the relationship between microplate motions and convecting mantle flow is unclear, there is a striking agreement between ongoing surface deformation evinced by GPS [*Wallace et al*., 2012] and our shear wave splitting results. Fast axes of the anisotropy mostly align closely with the geodetic velocity vectors and the region in the southeast where the lowest GPS velocities are observed is also the area where splitting is anomalous, weak, or unclear. Overall, the mantle fabric predicted by the modern strain field (Figure 10a) is extremely similar to the anisotropy that we observe.

Rayleigh-wave phase velocities show a swath of slow upper-mantle material that we infer to represent the rift axis, in agreement with heat flow [*Martinez and Goodliffe*, 2001], body wave tomography [*Abers et al*., 2002], and the location of the volcanoes. The lowest velocities likely represent flowing asthenosphere. Coherent, spreading-parallel fast axes observed on the DI indicate that an LPO has developed in the shallow convecting mantle in response to extension beneath, and adjacent to, the rift axis.

5.1.2. Asymmetry in Apparent Anisotropy

There is a distinct asymmetry to the splitting results; splitting in the north and beneath the DI is coherent and strong, while some anomalous splitting is observed to the south of the DI (Figure 8). This pattern may be enhanced by uneven distribution of the sensors, but overall the region is well sampled. It is unlikely to be a product of differential station noise; the stations in the interior of the Papuan Peninsula that show complex anisotropy are not noisier than the island stations which show simple anisotropy.

Rather, we interpret that north of $\sim$10°S large strains at depth have recently produced a strong extension-dominated fabric, while the relatively undeformed continent to the south of the parallel has much less clear structure. This is strongly supported by surface wave phase velocity maps, which indicate thinned lithosphere in an E-W swath between 9 and 10°S that extends from the DI beneath Cape Vogel, where splitting is predominantly N-S (Figure 9). A corollary is that significant extension has taken place within the Papuan Peninsula north of $\sim$10°S, roughly corresponding to the active Goodenough and Mai'iu fault structures (Figure 2), which explains the appreciable splitting times observed at stations on Cape Vogel. It is not clear whether this represents a wholesale southward jump of the crustal extension, or if it simply relates to distributed deformation within the weak continent.

An alternative cause of the asymmetry, which would also explain the significant splitting at the rift axis itself, is asymmetric mantle upwelling at depth due to relative motion of the rift axis in the hot spot reference frame (Figure 11). The south flank of the rift is moving northward with the Australian plate at $\sim$50 mm/yr, but the north flank moves northward faster. Thus, material upwelling beneath the axis must have come from the north, resulting in a thicker anisotropic region beneath the northern flank [cf. *Conder et al*., 2002; *Toomey et al*., 2002]. A similar interpretation has been suggested for shear wave splitting observations across the East Pacific Rise [*Hammond and Toomey*, 2003]; like our data set, those results evince significant splitting beneath the spreading axis and asymmetric splitting times, with larger δt in the direction the rift is moving. This configuration may explain our large splitting times beneath the rift axis and clearer anisotropy in the north than the south. Asymmetric spreading rates are also shown to produce asymmetric dips in the lithosphere-asthenosphere boundary (LAB) on the flanks of the rift [*Hammond and Toomey*, 2003], with a steeper LAB on the slower-spreading side; *Holtzman and Kendall* [2010] suggest that melt organized along the flank with a steeply dipping LAB could cause shear wave splitting with a fast axis parallel to the rift. This mechanism provides a possible explanation for the rift-parallel splitting we observe within and around the Goodenough Basin, on the slower, southern margin of the rift. However, this conjecture is difficult to test, and there is no evidence in the body wave tomography or the surface wave inversions for asymmetric LAB gradients.

5.1.3. Alternative Contributions to Anisotropy

Shear wave splitting observations suffer from a lack of depth resolution. We have ascribed observed splitting to olivine LPO arising from dislocation creep in the shallow, convecting mantle, but must rule out alternative sources of anisotropy. We observe consistent splitting from different back azimuths and between SKS and SKKS arrivals, implying the source of anisotropy in our field area is not in the deep mantle. We discuss some possibilities here (Figure 10).

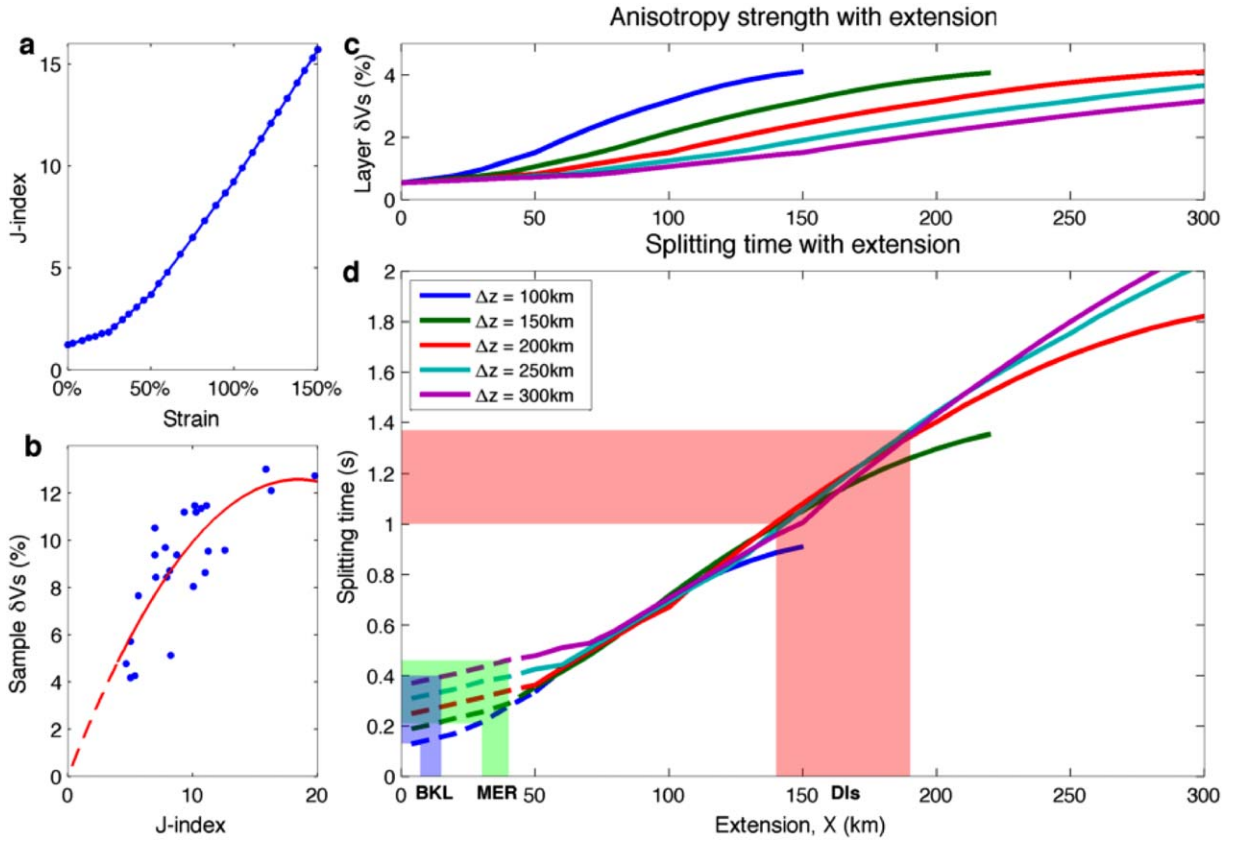

Figure 11. Calculation of anisotropy and splitting time as a function of surface displacement, *X*, at different thicknesses, Δz, of layer being sheared. (a) The relationship between γ and *J* index [from *Tommasi et al*., 2000]. (b) The relationship between *J* index and sample *Vs* anisotropy observed in naturally deformed olivine aggregates [blue dots, *Ismaïl and Mainprice*, 1998] and a quadratic polynomial fit to them (red line, dashed line indicates extrapolation) constrained to pass through [0,0]. (c) Strength of anisotropy within the layer increases with extension (*X*, in km) but decreases with layer thickness Δz. Line colors indicate Δz following key in Figure 11d. Anisotropy described as $\delta V_S/V_S$, the fractional difference between fast *S* and slow *S* wavespeed, assuming vertically propagating shear waves and horizontal fast axes. (d) Predicted splitting times, δt, due to LPO as a function of extension. Dashed lines indicate extrapolation of δV_S (*J*) beyond limits of data. Approximate values of extension and the predicted splitting times from LPO alone are shown for Baikal (BKL), the Main Ethiopian Rift (MER), and the D'Entrecasteaux Islands (DIs). Fits in Figures 11a and 11b used to generate models in Figure 11c.

Debayle et al. [2005] suggest that the ~50 mm/yr northward motion of Australia in the hot spot reference frame could produce a N-S fabric in sublithospheric mantle due to basal shear (Figure 10b). However, *SK(K)S* studies of the Australian continent yield little to no splitting [*Clitheroe and Van Der Hilst*, 1998; *Özalaybey and Chen*, 1999]. Robustly null splitting measured at the nearby PMG station (Figure 2) implies that any shearing-related fabric beneath the leading edge of Australia does not produce coherent splitting and bolsters our hypothesis that organized anisotropy within our array is the result of local structure.

There may also be an anisotropic contribution from the mantle lithosphere, resulting from plate stretching [cf. *Tommasi et al*., 1999] or "frozen-in" from previous deformation (Figure 10c). The robustly null splitting at PMG indicates that coherent lithospheric fossil fabric does not pervade across most of this region. Moreover, the absence of thick lithosphere beneath the DI inferred from mantle seismic velocities [*Abers et al*., 2002] (Figure 9) indicates that splitting observed throughout much of the array cannot have a lithospheric component.

Despite presumed upwelling and active volcanism, melt does not appear to have a great influence on the overall pattern of anisotropy. Melt pocket SPO or melt-modified LPO are predicted to result in extension-perpendicular fast axes (Figure 10d), strongest where asthenosphere comes closest to surface and solidus temperatures are most likely to be exceeded [*Blackman and Kendall*, 1997; *Holtzman et al*., 2003], whereas our results evince a dominantly extension-parallel fast direction beneath much of the DI, in the volcanically active region. As discussed above, melt channeled along a dipping LAB may contribute to complex fabrics south of 10°S, but any such melt zone is offset from volcanoes and otherwise not imaged.

Brownlee et al. [2011] anticipated that crustal anisotropy might be a diagnostic test for the mechanism of UHP exhumation because diapirism and low-angle detachment would produce distinct patterns of foliation within the domes. Our observations do not have the resolution to differentiate between the two alternatives, and predicted crustal δt of $\leq$0.4 s (based on velocities from *Brownlee et al*. [2011] and thicknesses from *Ferris et al*. [2006]) would likely be overwhelmed by the mantle splitting signal.

Present-day subduction at the New Britain and San Cristobal trenches $\sim$500 km to the north of the rift axis might affect local mantle dynamics, but these slabs dip northward, so associated return flow is not likely to complicate the signature of extension-related flow within the Woodlark Rift.

Notwithstanding complex recent tectonics, and ongoing UHP exhumation, the observed splitting is mostly simple. Beneath the DI, we do not find evidence for more exotic contributions to splitting, such as radial flow around exhuming diapirs (Figure 10e) [cf. *Behn et al*., 2007] or along-axis flow of a felsic nappe such as that proposed in the models of *Ellis et al*. [2011] (Figure 10f). Although such flow may take place, it is not sufficient to alter the predominant extension-parallel fabric caused by the large-scale extension-driven flow.

5.1.4. Second-Order Complexities in the South

Some stations, particularly in the south of our array, do not agree with the overall extension-parallel trend we have identified. On west Normanby Island the active Dawson Strait volcanic field may be obscuring signal from mantle anisotropy at stations ESA2 and MAYA, which show null or unclear splitting. Similarly WANI, which shows a large discrepancy between SI and SC results, is adjacent to the active stratovolcano Mt. Victory. Several stations in and around the Goodenough Basin show a bimodal distribution of $\sim$N-S and $\sim$ESE-WNW fast axes (Figure 7) although the station stacks give roughly ESE-WNW axes (Figure 8). Complex splitting such as this may arise from a layered anisotropic structure beneath the stations [*Silver and Savage*, 1994]. We have insufficient measurements to quantitatively model any layering, but can qualitatively assert a shallow contribution from melt (perhaps organized along a dipping LAB, see section 5.1.2) or along-axis flow as proposed by *Ellis et al*. [2011]. GOGO, which evinced large δt_{SI} despite several null individual arrivals, lies further from the rift axis, where extension is presumed to be minimal. We speculate that complex splitting here may be a result of preexisting fabric in continent that has not experienced large extension.

5.2. Broader Implications

5.2.1. A Quantitative Treatment of Strain-Induced Anisotropy

Experimental studies indicate that the strength of LPO fabric (defined by the dimensionless fabric strength index factor *J*, which quantifies the spread of the grain orientations) [*Bunge and Morris*, 1982], is related to the magnitude of strain (axial strain, ε, or shear strain, γ) a rock has undergone. At low strains, this produces an approximately linear increase in anisotropy with strain [*Mainprice and Silver*, 1993]. At larger strains (γ = 200–300%) seismic anisotropy asymptotes to a maximum due to diminishing increase in both fabric strength with strain and anisotropy with fabric strength [*Ismaïl and Mainprice*, 1998; *Tommasi et al*., 2000]. *Ismaïl and Mainprice* [1998] showed that 5–10% anisotropy on the hand-sample scale is produced by moderate fabrics (*J* factor $\geq$ 5) resulting from $\sim$50% equivalent strain in experiments [e.g., *Mainprice and Silver*, 1993] or viscoplastic self-consistent (VPSC) simulations [*Tommasi et al*., 2000]. These studies calibrate the relationship between anisotropy strength and *J*, and between ε (or γ) and *J*, providing an approximate relationship between finite strain and anisotropy.

We assume the extension (*X*) across the D'Entrecasteaux has caused a simple shear over some depth in the low-viscosity sublithospheric mantle (Figure 11). The magnitude of shear strain (γ) will vary inversely with the thickness of the layer (Δz) over which *X* is accommodated, since $\gamma = X/\Delta z$. Hence, we expect a larger Δz will give rise to a less strong fabric for a given *X*, and weaker LPO. However, for given anisotropy, a larger Δz will cause a larger accumulated splitting time for subvertical raypaths. The trade-off between these two effects depends on the gradients of the strain-fabric-anisotropy relationships.

For several possible values of Δz, we calculate γ as a function of *X*, and then use results from VPSC simulations of simple shear [*Tommasi et al*., 2000] to estimate *J* factor (Figure 12a). We convert *J* factor to Vs anisotropy (Figure 12b) using the relationships in the Olivine Fabric Database [*Ismaïl and Mainprice*, 1998], making the assumption that hand-sample anisotropy is typically three times than that of km-scale volumes of rock [*Christensen*, 2004], to estimate anisotropy as a function of *X* at different Δz (Figure 12c). We then compute predicted δt, assuming an average shear-wave velocity of 4.5 km/s (Figure 12d). For shear strains between $\sim$30 and 130% and $X \leq$ 200 km, there is little dependency of δt on Δz, such that the curves of $\delta t(X)$ at

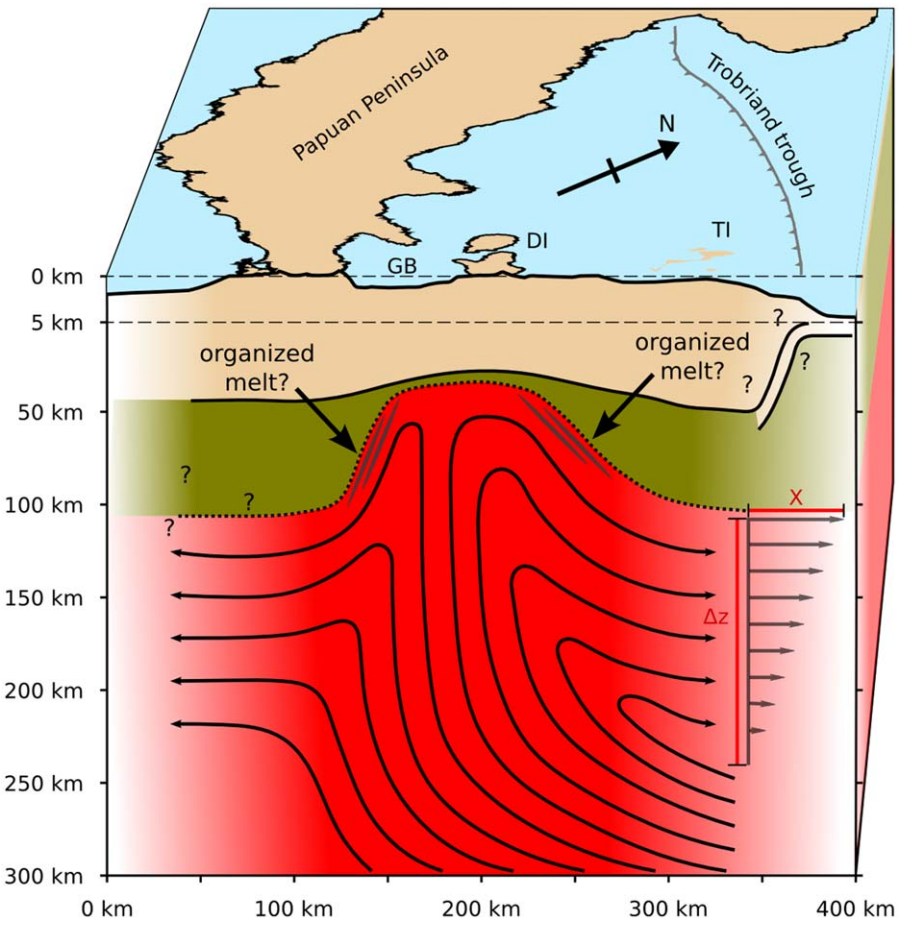

Figure 12. Cartoons depicting lithospheric extension and mantle flow beneath the D'Entrecasteaux Islands, including potential asymmetric flow pattern at depth due to relative motion of spreading axis in hot spot reference frame. Surface elevation taken from topography, crustal thickness is approximated from receiver functions [*Abers et al*., 2012] and lithospheric thinning estimated from δVp/Vp from body wave tomography [*Abers et al*., 2002]. Arrows indicate notional streamlines, in the frame of reference of the axis [cf. *Conder et al*., 2002]. Column at right shows 1-D strain field from *X* horizontal displacement accommodated over depth Δz (see Figure 11). In both the north and south, the influence of past subduction on the lithosphere geometry at depth is uncertain, and structures with question marks are unconstrained. Possible organized melt pockets result from porosity/viscosity gradients at the inclined base of the lithosphere [cf. *Holtzman and Kendall*, 2010]. Vertical-scale changes at 5 km; below this depth there is no vertical exaggeration. DI: D'Entrecasteaux Islands, GB: Goodenough Basin, and TI: Trobriand Islands. Tan shading: crust, green shading: lithospheric mantle, and red shading: asthenospheric mantle.

different values of Δz collapse onto a common line. In other words, the decrease in fabric strength is balanced by the increase in raypath length. Therefore, we can predict the magnitude of splitting without good constraints on the thickness of the anisotropic low-viscosity region. We calculate that 140–190 km of extension at the longitude of the DI should give rise to splitting times of 1–1.4 s. This independent constraint agrees well with the splitting magnitudes we observe, and provides quantitative support for the hypothesis that the observed anisotropy can be explained wholly by the recent extension.

5.2.2. Comparison With Other Rifts

We may compare our splitting observations to those from other regions of continental rifting, such as Baikal, the MER, or the Rio Grande Rift. Baikal evinces complex splitting close to the rift axis [*Gao et al*., 1997] and the MER is categorized by almost exclusively rift-parallel splitting fast directions [*Kendall et al*., 2005]. These two patterns are attributed, respectively, to small-scale mantle convection [*Gao*, 2003] and oriented melt pockets (OMP) [*Bastow et al*., 2010] or segregated melt bands [*Holtzman and Kendall*, 2010] within the lithosphere. Fast axes of splitting within the Rio Grande Rift are also parallel to the rift axis [*Sandvol et al*., 1992]. Our results do not resemble any of these rifts: while there is a small region with complex splitting, the majority of results indicate fast directions parallel to spreading.

Both Baikal and the MER have undergone relatively little total extension, at slow rates. Baikal has accumulated ~10.5 km [*Lesne et al*., 2000] to 9 km [*Zorin and Cordell*, 1991] of extension at 3–5 mm/yr since the mid-Pliocene, while the MER has accommodated ~30–40 km of Nubian-Somalian separation at rates of no more than 7–8 mm/yr [*Corti*, 2009] and broadly distributed extension across Rio Grande is ongoing at just ~1 mm/yr [*Berglund et al*., 2012]. As a result, lithospheric structures dominate seismic anisotropy. By contrast, 140–190 km of extension has taken place across the DI in <6 Myr, setting it apart from the other two rifts; seismic anisotropy beneath this rift is controlled by asthenospheric flow fabrics. Calculations (Figure 11) indicate that as a result of the disparity in extension, shear wave splitting times caused by extension-induced LPO at Baikal or the MER would be difficult to measure (<0.4 s), while they would be appreciable across the DI (Figure 11d). Plate stretching in this relatively magma-poor setting might add a lithospheric component to the anisotropy, but thin lithosphere beneath the rift axis limits this contribution (section 5.1.3).

If small-strain continental rifts represent one end-member extensional regime, the other end-member is a mid-ocean ridge (MOR). Shear wave splitting studies at MOR's have shown spreading-parallel fast directions [e.g., *Wolfe and Solomon*, 1998; *Nowacki et al*., 2012] albeit with some complexity at the axis. At some point on the continuum of continental breakup, the dominant anisotropic fabric within the rift must make the transition from the spreading-perpendicular trend observed at small-strain rifts to the spreading-parallel trend seen at MORs; Figure 11 offers a way to quantify this transition. Our interpretation is that the Woodlark rift has evolved to the spreading-parallel fabric, and provides an upper bound on the minimum extension required for a predominating LPO.

The relatively narrow surface expression of the Woodlark Rift indicates that well-understood strain localizing processes are at work [*Buck*, 1991] and that extension in the lithosphere seems to be localized [*Abers et al*., 2002]. However, within the Trobriand Platform, our results indicate strong, coherent spreading-parallel anisotropy at distances >100 km from the rift axis notwithstanding a lack of crustal faulting. This implies that organized structure at depth precedes surface extension. We infer that a region of convecting mantle wider than the surficial rift is affected by the extension and that tectonic strain becomes more diffuse as it is distributed to depth.

6. Conclusions

Shear wave splitting reveals a preponderance of extension-parallel fast axes in this young, continental rift system, contrary to results from less-extended rifts, such as Ethiopia or Baikal. The Woodlark-D'Entrecasteaux Rift represents an intermediate stage in the evolution between a small-extension intracontinental rift and an oceanic spreading center. The observed anisotropy indicates that the concomitant transition in mantle fabric has already taken place, from a fabric possibly dominated by melt or preexisting structure to an LPO controlled by the extension. The fabric change is a consequence of the magnitude of extension and demonstrates how efficiently deformation mechanisms establish LPO in the mantle as it accumulates shear strain. The observation of anisotropy beneath the undeformed Trobriand Plateau indicates that appreciable flow of convecting mantle may precede crustal deformation. Despite the proximate volcanic centers, our results do not require melt to make a significant contribution to the structure, although unexplained complexity in the southern part of the rift (where there is no volcanism) might be influenced by deep melt migrating along the rift margin or preexisting structure. Any model for UHP exhumation and extension across the D'Entrecasteaux Islands that is eventually preferred must be consistent with a simple, spreading-parallel fabric at depth.

Acknowledgments

We thank Roger Buck, Laura Wallace, and Susan Ellis for helpful comments and discussion during the course of this study, and we appreciate useful input from Suzanne Baldwin and two anonymous reviewers. We are grateful to Hugh Davies for facilitating the fieldwork, as well as to the IRIS-PASSCAL Instrument Center for providing instruments and field support. For the field deployment, we are indebted to the efforts of J. Calkins, P. Ruprecht, R. Buck, T. Koczynski, P. Irarue, and R. Verave (UPNG/MRA), J. Oa and E. Nidkambu (National Mapping). This research was supported by NSF grants EAR-0814236 (Abers) and EAR-0708445 (Gaherty).

References

Abers, G. A., C. Z. Mutter, and J. Fang (1997), Shallow dips of normal faults during rapid extension: Earthquakes in the Woodlark-D'Entrecasteaux rift system, Papua New Guinea, *J. Geophys. Res.*, *102*(B7), 15,301–15,307.

Abers, G. A., A. Ferris, M. Craig, H. L. Davies, A. L. Lerner-Lam, J. C. Mutter, and B. Taylor (2002), Mantle compensation of active metamorphic core complexes at Woodlark rift in Papua New Guinea, *Nature*, *418*(6900), 862–865.

Abers, G. A., Y. H. Kim, J. B. Gaherty, Z. Eilon, G. Jin, and R. Verave (2012), Imaging to understand exhumation of UHP rocks during rifting: The 2010–2011 CD Papua seismic experiment, Abstract T42C-06 presented at 2012 Fall Meeting, AGU, San Francisco, Calif.

Baker, G. E., and J. L. Stevens (2004), Backazimuth estimation reliability using surface wave polarization, *Geophys. Res. Lett.*, *31*, L09611, doi: 10.1029/2004GL019510.

Baldwin, S. L., B. D. Monteleone, L. E. Webb, P. G. Fitzgerald, M. Grove, and E. June Hill (2004), Pliocene eclogite exhumation at plate tectonic rates in eastern Papua New Guinea, *Nature*, *431*(7006), 263–267, doi:10.1038/nature02846.

Baldwin, S. L., L. E. Webb, and B. D. Monteleone (2008), Late Miocene coesite-eclogite exhumed in the Woodlark Rift, *Geology*, *36*(9), 735–738, doi:10.1130/G25144A.1;4figures;DataRepositoryitem2008184.
Baldwin, S. L., P. G. Fitzgerald, and L. E. Webb (2012), Tectonics of the New Guinea Region, *Annu. Rev. Earth Planet. Sci.*, *40*, 495–520, doi:10.1146/annurev-earth-040809-152540.
Bastow, I. D., S. Pilidou, J. M. Kendall, and G. W. Stuart (2010), Melt-induced seismic anisotropy and magma assisted rifting in Ethiopia: Evidence from surface waves, *Geochem. Geophys. Geosyst.*, *11*, Q0AB05, doi:10.1029/2010GC003036.
Becker, T. W., B. Kustowski, and G. Ekström (2008), Radial seismic anisotropy as a constraint for upper mantle rheology, *Earth Planet. Sci. Lett.*, *267*(1–2), 213–227, doi:10.1016/j.epsl.2007.11.038.
Behn, M. D., G. Hirth, and P. B. Kelemen (2007), Trench-parallel anisotropy produced by foundering of arc lower crust, *Science*, *317*(5834), 108–111, doi:10.1126/science.1141269.
Berglund, H. T., A. F. Sheehan, M. H. Murray, M. Roy, A. R. Lowry, R. S. Nerem, and F. Blume (2012), Distributed deformation across the Rio Grande Rift, Great Plains, and Colorado Plateau, *Geology*, *40*(1), 23–26, doi:10.1130/G32418.1.
Blackman, D. K., and J. M. Kendall (1997), Sensitivity of teleseismic body waves to mineral texture and melt in the mantle beneath a mid-ocean ridge, *Philos. Trans. R. Soc. London A*, *355*(1723), 217–231, doi:10.1098/rsta.1997.0007.
Blackman, D. K., H. R. Wenk, and J. M. Kendall (2002), Seismic anisotropy of the upper mantle 1. Factors that affect mineral texture and effective elastic properties, *Geochem. Geophys. Geosyst.*, *3*(9), 8601, doi:10.1029/2001GC000248.
Bowman, J. R., and M. Ando (1987), Shear-wave splitting in the upper-mantle wedge above the Tonga subduction zone, *Geophys. J. Int.*, *88*(1), 25–41.
Brownlee, S. J., B. R. Hacker, M. Salisbury, G. Seward, T. A. Little, S. L. Baldwin, and G. A. Abers (2011), Predicted velocity and density structure of the exhuming Papua New Guinea ultrahigh-pressure terrane, *J. Geophys. Res.*, *116*, B08206, doi:10.1029/2011JB008195.
Buck, W. R. (1991), Modes of continental lithospheric extension, *J. Geophys. Res.*, *96*(20), 161–120.
Bunge, H. J., and P. R. Morris (1982), *Texture Analysis in Materials Science: Mathematical Methods*, Butterworths, London.
Chevrot, S. (2000), Multichannel analysis of shear wave splitting, *J. Geophys. Res.*, *105*(B9), 21,579–21,590.
Christensen, N. I. (1984), The magnitude, symmetry and origin of upper mantle anisotropy based on fabric analyses of ultramafic tectonites, *Geophys. J. Int.*, *76*(1), 89–111, doi:10.1111/j.1365-246X.1984.tb05025.x.
Christensen, N. I. (2004), Serpentinites, peridotites, and seismology, *Int. Geol. Rev.*, *46*(9), 795–816, doi:10.2747/0020-6814.46.9.795.
Clitheroe, G., and R. D. Van Der Hilst (1998), Complex anisotropy in the Australian lithosphere from shear-wave splitting in broad-band SKS records, in *Structure and Evolution of the Australian Continent*, edited by J. Braun et al., AGU, Washington, D. C., 73–78 doi:10.1002/9781118670095.ch5.
Conder, J. A., D. W. Forsyth, and E. M. Parmentier (2002), Asthenospheric flow and asymmetry of the East Pacific Rise, MELT area, *J. Geophys. Res.*, *107*(B12), 2344, doi:10.1029/2001JB000807.
Corti, G. (2009), Continental rift evolution: From rift initiation to incipient break-up in the Main Ethiopian Rift, East Africa, *Earth Sci. Rev.*, *96*(1–2), 1–53, doi:10.1016/j.earscirev.2009.06.005.
Davies, H. L., and R. G. Warren (1988), Origin of eclogite-bearing, domed, layered metamorphic complexes (''core complexes'') in the D'Entrecasteaux islands, Papua New Guinea, *Tectonics*, *7* (1), 1–21.
Debayle, E., B. Kennett, and K. Priestly (2005), Global azimuthal seismic anisotropy and the unique plate-motion deformation of Australia, *Nature*, *433*(7025), 509–512.
DeMets, C., R. G. Gordon, D. F. Argus, and S. Stein (1994), Effect of recent revisions to the geomagnetic reversal time scale on estimates of current plate motions, *Geophys. Res. Lett.*, *21*(20), 2191–2194.
Ellis, S. M., T. A. Little, L. M. Wallace, B. R. Hacker, and S. J. H. Buiter (2011), Feedback between rifting and diapirism can exhume ultrahigh-pressure rocks, *Earth Planet. Sci. Lett.*, *311*(3–4), 427–438, doi:10.1016/j.epsl.2011.09.031.
Ferris, A., G. A. Abers, B. Zelt, B. Taylor, and S. W. Roecker (2006), Crustal structure across the transition from rifting to spreading: The Woodlark rift system of Papua New Guinea, *Geophys. J. Int.*, *166*(2), 622–634, doi:10.1111/j.1365-246X.2006.02970.x.
Foley, B. J., and M. D. Long (2011), Upper and mid-mantle anisotropy beneath the Tonga slab, *Geophys. Res. Lett.*, *38*, L02303, doi:10.1029/2010GL046021.
Fouch, M. J., and K. M. Fischer (1996), Mantle anisotropy beneath northwest Pacific subduction zones, *J. Geophys. Res.*, *101*(B7), 15,987–16,002, doi:10.1029/96JB00881.
Francis, G., J. Lock, and Y. Okuda (1987), Seismic stratigraphy and structure of the area to the southeast of the Trobriand Platform, *Geo Mar. Lett.*, *7*(3), 121–128.
Gaboret, C., A. M. Forte, and J. P. Montagner (2003), The unique dynamics of the Pacific Hemisphere mantle and its signature on seismic anisotropy, *Earth Planet. Sci. Lett.*, *208*(3), 219–233.
Gao, S. S. (2003), Evidence for small-scale mantle convection in the upper mantle beneath the Baikal rift zone, *J. Geophys. Res.*, *108*(B4), 2194, doi:10.1029/2002JB002039.
Gao, S. S., P. M. Davis, H. Liu, P. D. Slack, A. W. Rigor, Y. A. Zorin, V. V. Mordvinova, V. M. Kozhevnikov, and N. A. Logatchev (1997), SKS splitting beneath continental rift zones, *J. Geophys. Res.*, *102*(B10), 22,781–22,797.
Goodliffe, A. M., and B. Taylor (2007), The boundary between continental rifting and sea-floor spreading in the Woodlark Basin, Papua New Guinea, *Geol. Soc. Spec. Publ.*, *282*(1), 217–238.
Goodliffe, A. M., B. Taylor, and F. Martinez (1999), Data report: Marine geophysical surveys of the Woodlark Basin region, in *Proc. Ocean Drill. Program Initial Rep.*, vol. *180*, edited by B. Taylor et al., pp. 1–20, U.S. Gov. Print. Off., Washington, D. C.
Gordon, S. M., T. A. Little, B. R. Hacker, S. A. Bowring, M. Korchinski, S. L. Baldwin, and A. R. C. Kylander-Clark (2012), Multi-stage exhumation of young UHP-HP rocks: Timescales of melt crystallization in the D'Entrecasteaux Islands, southeastern Papua New Guinea, *Earth Planet. Sci. Lett.*, *351–352*, 237–246, doi:10.1016/j.epsl.2012.07.014.
Hall, R., and W. Spakman (2002), Subducted slabs beneath the eastern Indonesia-Tonga region: Insights from tomography, *Earth Planet. Sci. Lett.*, *201*(2), 321–336.
Hammond, W. C., and D. R. Toomey (2003), Seismic velocity anisotropy and heterogeneity beneath the Mantle Electromagnetic and Tomography Experiment (MELT) region of the East Pacific Rise from analysis of Pand Sbody waves, *J. Geophys. Res.*, *108*(B4), 2176, doi:10.1029/2002JB001789.
Hill, E., S. L. Baldwin, and G. S. Lister (1992), Unroofing of active metamorphic core complexes in the D'Entrecasteaux Islands, Papua New Guinea, *Geology*, *20*(10), 907–910.
Hill, K. C., and R. Hall (2003), Mesozoic-Cenozoic evolution of Australia's New Guinea margin in a west Pacific context, *Geol. Soc. Am. Spec. Pap.*, *372*, 265–290.

Holtzman, B. K., and J. M. Kendall (2010), Organized melt, seismic anisotropy, and plate boundary lubrication, *Geophys. Geochem. Geosyst.*, *11*, Q0AB06, doi:10.1029/2010GC003296.
Holtzman, B. K., D. L. Kohlstedt, and M. E. Zimmerman (2003), Melt segregation and strain partitioning: Implications for seismic anisotropy and mantle flow, *Science*, *301*(5637), 1227–1230.
Ismaïl, W. B., and D. Mainprice (1998), An olivine fabric database: An overview of upper mantle fabrics and seismic anisotropy, *Tectonophysics*, *296*(1–2), 145–157.
Jin, G., J. B. Gaherty, G. A. Abers, Y. H. Kim, Z. Eilon, W. R. Buck, and R. Verave (2013), Surface wave tomography of D'Entrecasteaux Islands, Papua New Guinea, implication of mantle control on localization of extension and exhumation, Abstract T21B-2554 presented at 2013 Fall Meeting, AGU, San Francisco, Calif.
Kendall, J. M., G. W. Stuart, C. J. Ebinger, I. D. Bastow, and D. Keir (2005), Magma-assisted rifting in Ethiopia, *Nature*, *433*(7022), 146–148.
Kington, J. D., and A. M. Goodliffe (2008), Plate motions and continental extension at the rifting to spreading transition in Woodlark Basin, Papua New Guinea: Can oceanic plate kinematics be extended into continental rifts?, *Tectonophysics*, *458*(1–4), 82–95, doi:10.1016/j.tecto.2007.11.027.
Lesne, O., E. Calais, J. Deverchère, J. Chéry, and R. Hassani (2000), Dynamics of intracontinental extension in the north Baikal rift from two-dimensional numerical deformation modeling, *J. Geophys. Res.*, *105*(B9), 21,727–21,744, doi:10.1029/2000JB900139.
Levin, V., D. Droznin, J. Park, and E. Gordeev (2004), Detailed mapping of seismic anisotropy with local shear waves in southeastern Kamchatka, *Geophys. J. Int.*, *158*(3), 1009–1023.
Little, T. A., S. L. Baldwin, P. G. Fitzgerald, and B. Monteleone (2007), Continental rifting and metamorphic core complex formation ahead of the Woodlark spreading ridge, D'Entrecasteaux Islands, Papua New Guinea, *Tectonics*, *26*, TC1002, doi:10.1029/2005TC001911.
Little, T. A., B. R. Hacker, S. M. Gordon, S. L. Baldwin, P. G. Fitzgerald, S. M. Ellis, and M. Korchinski (2011), Diapiric exhumation of Earth's youngest (UHP) eclogites in the gneiss domes of the D'Entrecasteaux Islands, Papua New Guinea, *Tectonophysics*, *510*(1–2), 39–68, doi:10.1016/j.tecto.2011.06.006.
Long, M. D., and P. G. Silver (2009), Shear wave splitting and mantle anisotropy: Measurements, interpretations, and new directions, *Surv. Geophys.*, *30*(4–5), 407–461.
Long, M. D., and R. D. Van Der Hilst (2005), Estimating shear-wave splitting parameters from broadband recordings in Japan: A comparison of three methods, *Bull. Seismol. Soc. Am.*, *95*(4), 1346–1358.
Long, M. D., M. H. Benoit, and M. C. Chapman (2010), Upper mantle anisotropy and transition zone thickness beneath southeastern North America and implications for mantle dynamics, *Geochem. Geophys. Geosyst.*, *11*, Q10012, doi:10.1029/2010GC003247.
Mainprice, D., and P. G. Silver (1993), Interpretation of SKS-waves using samples from the subcontinental lithosphere, *Phys. Earth Planet. Inter.*, *78*(3), 257–280.
Mann, P., B. K. Horton, F. W. Taylor, C. Shen, K. Lin, and W. Renema (2009), Uplift patterns of reef terraces and sedimentary rocks constrain tectonic models for metamorphic core complexes in eastern Papua New Guinea, *Eos Trans. AGU*, *90*(52), Fall Meet. Suppl., Abstract G33B-0642.
Martinez, F., and A. M. Goodliffe (2001), Metamorphic core complex formation by density inversion and lower-crust extrusion, *Nature*, *411*, 930–934.
Miller, S. R., S. L. Baldwin, and P. G. Fitzgerald (2012), Transient fluvial incision and active surface uplift in the Woodlark Rift of eastern Papua New Guinea, *Lithosphere*, *4*(2), 131–149.
Nowacki, A., J. M. Kendall, and J. Wookey (2012), Mantle anisotropy beneath the Earth's mid-ocean ridges, *Earth Planet. Sci. Lett.*, *317*, 56–67.
Ollier, C. D., and C. F. Pain (1980), Actively rising surficial gneiss domes in Papua New Guinea, *J. Geol. Soc. Aust.*, *27*(1–2), 33–44, doi:10.1080/00167618008729116.
Özalaybey, S., and W. P. Chen (1999), Frequency-dependent analysis of SKS/SKKS waveforms observed in Australia: Evidence for null birefringence, *Phys. Earth Planet. Inter.*, *114*(3–4), 197–210.
Pegler, G., S. Das, and J. H. Woodhouse (1995), A seismological study of the eastern New Guinea and the western Solomon Sea regions and its tectonic implications, *Geophys. J. Int.*, *122*(3), 961–981.
Restivo, A., and G. Helffrich (1999), Teleseismic shear wave splitting measurements in noisyenvironments, *Geophys. J. Int.*, *137*(3), 821–830, doi:10.1046/j.1365-246x.1999.00845.x.
Sandvol, E., J. Ni, S. Ozalaybey, and J. Schlue (1992), Shear-wave splitting in the Rio Grande Rift, *Geophys. Res. Lett*, *19*(23), 2337–2340, doi:10.1029/92GL02715.
Silver, P. G., and W. W. Chan (1991), Shear wave splitting and subcontinental mantle deformation, *J. Geophys. Res.*, *96*(B10), 16,429–16,454.
Silver, P. G., and M. D. Long (2011), The non-commutivity of shear wave splitting operators at low frequencies and implications for anisotropy tomography, *Geophys. J. Int.*, *184*(3), 1415–1427, doi:10.1111/j.1365-246X.2010.04927.x.
Silver, P. G., and M. K. Savage (1994), The interpretation of shear-wave splitting parameters in the presence of two anisotropic layers, *Geophys. J. Int.*, *119*(3), 949–963, doi:10.1111/j.1365-246X.1994.tb04027.x.
Smith, I. E., and J. S. Milsom (1984), Late Cenozoic volcanism and extension in Eastern Papua, *Geol. Soc. Spec. Publ.*, *16*(1), 163–171, doi:10.1144/GSL.SP.1984.016.01.12.
Smith, I. E. M., and R. W. Johnson (1981), Contrasting rhyolite suites in the Late Cenozoic of Papua New Guinea, *J. Geophys. Res.*, *86*(B11), 10,257–10,272, doi:10.1029/JB086iB11p10257.
Smith, G. P., D. A. Wiens, K. M. Fischer, L. M. Dorman, S. C. Webb, and J. A. Hildebrand (2001), A Complex Pattern of Mantle Flow in the Lau Backarc, *Science*, *292*(5517), 713–716, doi:10.1126/science.1058763.
Soedjatmiko, B., and N. I. Christensen (2000), Seismic anisotropy under extended crust: Evidence from upper mantle xenoliths, Cima Volcanic Field, California, *Tectonophysics*, *321*(3), 279–296, doi:10.1016/S0040-1951(00)00070-6.
Stachnik, J. C., A. F. Sheehan, D. W. Zietlow, Z. Yang, J. Collins, and A. Ferris (2012), Determination of New Zealand ocean bottom seismometer orientation via Rayleigh-wave polarization, *Seismol. Res. Lett.*, *83*(4), 704–713, doi:10.1785/0220110128.
Stolz, A. J., G. R. Davies, A. J. Crawford, and I. E. M. Smith (1993), Sr, Nd und Pb Isotopenzusammensetzung saurer kalkalkalischer und peralkalischer Vulkanite der D' Entrecasteaux Inseln, Papua Neuguinea, und ihre tektonische Bedeutung, *Mineral. Petrol.*, *47*(2–4), 103–126, doi:10.1007/BF01161562.
Taylor, B., A. M. Goodliffe, and F. Martinez (1999), How continents break up: Insights from Papua New Guinea, *J. Geophys. Res.*, *104*(B4), 7497–7512.
Tommasi, A., B. Tikoff, and A. Vauchez (1999), Upper mantle tectonics: Three-dimensional deformation, olivine crystallographic fabrics and seismic properties, *Earth Planet. Sci. Lett.*, *168*(1), 173–186.

Tommasi, A., D. Mainprice, G. Canova, and Y. Chastel (2000), Viscoplastic self-consistent and equilibrium-based modeling of olivine lattice preferred orientations—Implications for the upper mantle seismic anisotropy, *J. Geophys. Res.*, *105*(B4), 7893–7908.
Toomey, D. R., W. Wilcock, and J. A. Conder (2002), Asymmetric mantle dynamics in the MELT region of the East Pacific Rise, *Earth Planet. Sci. Lett.*, *200*(3–4), 287–295.
Tregoning, P., K. Lambeck, and A. Stolz (1998), Estimation of current plate motions in Papua New Guinea from Global Positioning System observations, *J. Geophys. Res.*, *103*(B6), 12,181–12,203.
Vecsey, L., J. Plomerová, and V. Babuska (2008), Shear-wave splitting measurements—Problems and solutions, *Tectonophysics*, *462*(1–4), 178–196.
Vidale, J. E. (1986), Complex polarization analysis of particle motion, *Bull. Seismol. Soc. Am.*, *76*(5), 1393–1405.
Wallace, L. M., et al. (2004), GPS and seismological constraints on active tectonics and arc-continent collision in Papua New Guinea: Implications for mechanics of microplate rotations in a plate boundary zone, *J. Geophys. Res.*, *109*, B05404, doi:10.1029/2003JB002481.
Wallace, L. M., S. M. Ellis, P. Tregoning, T. A. Little, and N. Palme (2012), Distribution of contemporary crustal deformation and mechanisms for extension in the Woodlark Rift: Insights from GPS, Abstract T42C-04 presented at 2012 Fall Meeting, AGU, San Francisco, Calif.
Webb, L. E., S. L. Baldwin, and T. A. Little (2008), Can microplate rotation drive subduction inversion?, *Geology*, *36*(10), 823–826, doi: 10.1130/G25134A.1.
Webb, S. C. (1998), Broadband seismology and noise under the ocean, *Rev. Geophys.*, *36*(1), 105–142.
Webb, S. C., and W. C. Crawford (2010), Shallow-water broadband OBS seismology, *Bull. Seismol. Soc. Am.*, *100*(4), 1770–1778, doi:10.1785/0120090203.
Weissel, J. K., B. Taylor, and G. D. Karner (1982), The opening of the Woodlark Basin, subduction of the Woodlark spreading system, and the evolution of northern Melanesia since mid-Pliocene time, *Tectonophysics*, *87*(1–4), 253–277.
Wolfe, C. J., and P. G. Silver (1998), Seismic anisotropy of oceanic upper mantle: Shear wave splitting methodologies and observations, *J. Geophys. Res.*, *103*(B1), 749–771, doi:10.1029/97JB02023.
Wolfe, C. J., and S. C. Solomon (1998), Shear-wave splitting and implications for mantle flow beneath the MELT region of the East Pacific Rise, *Science*, *280*(5367), 1230–1232.
Wüstefeld, A., G. Bokelmann, C. Zaroli, and G. Barruol (2008), SplitLab: A shear-wave splitting environment in Matlab, *Comput. Geosci.*, *34*, 515–528.
Yang, X., K. M. Fischer, and G. A. Abers (1995), Seismic anisotropy beneath the Shumagin Islands segment of the Aleutian-Alaska subduction zone, *J. Geophys. Res.*, *100*(B9), 18,165–18,177, doi:10.1029/95JB01425.
Zirakparvar, N. A., S. L. Baldwin, and J. D. Vervoort (2011), Lu-Hf garnet geochronology applied to plate boundary zones: Insights from the (U)HP terrane exhumed within the Woodlark Rift, *Earth Planet. Sci. Lett.*, *309*(1–2), 56–66, doi:10.1016/j.epsl.2011.06.016.
Zorin, Y., and L. Cordell (1991), Crustal extension in the Baikal rift zone, *Tectonophysics*, *198*(1), 117–121.